

Copyright © 1991, by the author(s).  
All rights reserved.

Permission to make digital or hard copies of all or part of this work for personal or classroom use is granted without fee provided that copies are not made or distributed for profit or commercial advantage and that copies bear this notice and the full citation on the first page. To copy otherwise, to republish, to post on servers or to redistribute to lists, requires prior specific permission.

**A TWO-COUPLED-SHEATH MODEL FOR THE  
CONDUCTION OF CURRENT THROUGH  
ASYMMETRIC PARALLEL PLATE RF DISCHARGES**

by

A. H. Sato and M. A. Lieberman

Memorandum No. UCB/ERL M91/81

25 September 1991

COVER PAGE

**A TWO-COUPLED-SHEATH MODEL FOR THE  
CONDUCTION OF CURRENT THROUGH  
ASYMMETRIC PARALLEL PLATE RF DISCHARGES**

by

A. H. Sato and M. A. Lieberman

Memorandum No. UCB/ERL M91/81

25 September 1991

**ELECTRONICS RESEARCH LABORATORY**

College of Engineering  
University of California, Berkeley  
94720

TITLE PAGE

**A TWO-COUPLED-SHEATH MODEL FOR THE  
CONDUCTION OF CURRENT THROUGH  
ASYMMETRIC PARALLEL PLATE RF DISCHARGES**

by

A. H. Sato and M. A. Lieberman

Memorandum No. UCB/ERL M91/81

25 September 1991

**ELECTRONICS RESEARCH LABORATORY**

College of Engineering  
University of California, Berkeley  
94720

# **A Two-Coupled-Sheath Model for the Conduction of Current Through Asymmetric Parallel Plate RF Discharges**

**A.H. Sato**

Department of Physics, University of California, Berkeley, California 94720

**M.A. Lieberman**

Department of Electrical Engineering and Computer Sciences  
University of California, Berkeley, California 94720

## **ABSTRACT**

The effect of electrode area ratio on the current flowing through a parallel plate rf discharge is studied to gain qualitative understanding of how current continuity is maintained in asymmetric systems and how electrode asymmetry affects the harmonic spectrum of the current. A uniform ion density sheath model is used. The total current flowing through the powered electrode sheath is equated to that at the grounded electrode sheath, and the external voltage is set equal to the sum of the voltage drops across each sheath. This results in a first order differential equation in one sheath voltage, which is integrated numerically. Some results are: (1) The current waveforms approach skewed sine waves with increasing area ratio. (2) Increasing the area ratio induces a broadening of both conduction and displacement current frequency spectra. (3) The relative size of the peak conduction current to the displacement current is important in determining the sheath voltage and current

waveforms. (4) Even when the peak conduction current is comparable to the peak displacement current, the large, distinct conduction current spike associated with the single sheath limit is very weak at modest area ratios. In this case, the coupling of two sheaths allows nonsinusoidal variations in the sheath voltages that broaden the conduction current waveform. (5) The response of the external circuit to the discharge current load must be included in a description of the total current waveform. Examples of these effects from experiment and simulation are discussed.

## I. Introduction

The impedance of rf discharges has been studied for many years and is important in the design of matching networks for rf discharge reactors.<sup>1</sup> It has also been studied for endpoint detection purposes in the fabrication of integrated circuits,<sup>2</sup> and has received extensive interest as a measurable quantity that can provide information of discharge parameters such as density, collision frequencies, and sheath thickness.<sup>3,4,5,6</sup> Directional wattmeters are often used to measure the power absorbed by the discharge, and at the matched load condition it is possible to infer a value for the discharge impedance.<sup>1</sup> However, measurements made with directional wattmeters can be complicated by matching network losses,<sup>7</sup> and consequently a correction for this power loss must be found by calibration.<sup>8,9,10</sup> Alternatively, workers have resorted to the direct measurement of the discharge voltage and current to obtain the discharge impedance and power, computing the latter by using the phase difference between the current and voltage,<sup>5</sup> using the time-averaged product of the current and voltage waveforms,<sup>11</sup> or employing the equivalent of the latter through the use of Fourier transforms.<sup>12</sup> Studies which have made direct use of the current and voltage waveforms tend to employ near symmetric discharges for which the higher harmonic content is small.<sup>5,6,10</sup> As has been noted in Ref. 10, power measurement in asymmetric discharges is complicated by the generation of higher harmonics, which makes it difficult to identify the phase shift at the fundamental. Power measurements in asymmetric systems are therefore best done by time-averaging the product of the current and voltage waveforms, and hence accurate measurements of the discharge voltage and current become essential.

However, one complication that is encountered experimentally is the question of what constitutes a valid current waveform in an asymmetric system. Experimental work has shown that current waveforms for asymmetric systems are marked by greater harmonic content,<sup>12</sup> and that in some reactor geometries conventional measurement techniques yield waveforms in which the harmonics are a dominating feature.<sup>13</sup> It has been recognized that the symmetric discharge possesses a symmetry that precludes the existence of even harmonics.<sup>14</sup> This requirement is absent

for asymmetric discharges. It is also known that in the uniform density sheath model of the symmetric discharge (with conduction current neglected), the two sheaths together act as a linear element.<sup>15</sup> We will show that this simple result does not persist in asymmetric discharges. Thus current waveforms for asymmetric systems are inherently more complicated, and it is important to develop some understanding of what is reasonable to expect in experiments.

In this paper we study the qualitative features of current conduction through asymmetric discharges with the use of a simple uniform sheath density model. For an overall description of an rf discharge this model is somewhat lacking; for example, the ion density profile in the sheaths can affect stochastic heating, which in turn can affect the steady state plasma density. But the question we address is much more limited. It is simply: How is current continuity achieved in asymmetric systems, and how does asymmetry affect the harmonic content of the current waveform? We will find that the appearance of more complex harmonic structure at large asymmetry follows naturally from this two-sheath model, and hence a study of this sort is important in defining constraints imposed on discharge symmetry if it is important to perform careful measurements of discharge impedance. In the past, models of this sort have also provided insight about how the sheath voltage modulates the conduction and displacement currents, and hence how current continuity provides a constraint between the sheath voltages at the two electrodes.<sup>16,17,18,19,20,21</sup> Meijer and Goedheer,<sup>21</sup> in particular, used the same model we present here, and found that it could reproduce experimental dc bias data. This work, in comparison, is primarily concerned with the current waveform.

The outline of this paper is as follows: The equations describing current continuity are formulated in Section II. Section III presents results and discussion concerning the discharge current. In Section IV the results of this model are related to previously published simulation results and experimental data. In Section V we show how features appearing in current waveforms we have measured may be better understood with the help of this two-coupled-sheath model. In Section VI we discuss the relation of this model to the purely resistive sheath model of Ref. 16.

## II. Model Description

### A. Two-Sheath System

The capacitively coupled rf discharge is illustrated in Figure 1(a). A sinusoidal rf voltage of amplitude  $V_1$  is applied to the powered electrode through a blocking capacitor  $C_{\text{block}}$ . In a system with an asymmetric electrode configuration, a dc current will flow in the circuit until a dc bias  $V_0$  forms across the blocking capacitor to prevent further flow of a dc current. The external voltage  $V_{\text{ext}}$  then appearing at the powered electrode is the sum of the dc bias and the sinusoidal voltage from the power supply.

The model for the sheath of a capacitive rf discharge is illustrated in Figure 1(b). The ion density profile  $n_i(x)$  will be treated as constant in time, which will be true when the rf frequency is larger than the ion plasma frequency--  $\omega^2 \gg \omega_{pi}^2$ --and the sheath is wide enough that an ion transit time is several rf periods long.<sup>22,23,24</sup> The electron density profile  $n_e(x,t)$  is approximated as changing abruptly from zero to the ion density at the instantaneous sheath edge  $s(t)$ . The sheath edge moves between a minimum near the electrode at  $x=0$  to a maximum position at  $x=x_m$ . The positive directions of the currents and voltages are indicated in Figure 1.

The conduction current is taken to be the sum of a steady ion flux and the rf modulated flux provided by Maxwellian electrons:

$$J_c(t) = -en_s u_B + (1/4)en_s c_e \exp(-eV_s(t)/kT) \quad (1)$$

where  $c_e = (8kT/\pi m_e)^{1/2}$  is the mean electron speed,  $n_s$  is the ion density at  $x_m$ , and  $e$  is the electron charge. The ions are given a speed  $u_B$  at  $x=x_m$ .  $V_s$  is the time-varying voltage at the plasma-sheath edge  $x=s(t)$  with respect to the electrode surface at  $x=0$ . (We assume here that  $V_s(t)$  is always positive. A limit on the applied rf voltage to ensure  $V_s > 0$  has been indicated in other works.<sup>25,26</sup>) The expression for the electron flux is inaccurate for very small sheath voltages, so some caution must be used in interpreting the waveforms near the sheath voltage minima.<sup>27</sup>

The displacement current is obtained by applying Gauss' law in the region  $0 < x < s(t)$  where the electron density is zero:

$$\partial E(x,t)/\partial x = en_i(x)/\epsilon_0 . \quad (2)$$

$E(x,t)$  is the electric field, and  $\epsilon_0$  is the permittivity of free space. The boundary condition for the electric field is

$$E(s,t) = 0 . \quad (3)$$

Integrating Eq. (2) and using Eq. (3), one obtains

$$E(x,t) = -\int_x^s dx' en_i(x')/\epsilon_0 . \quad (4)$$

The displacement current  $J_d$  is given by

$$\begin{aligned} J_d(x,t) &= \epsilon_0 \partial E / \partial t \\ &= -en_i(s) \frac{ds}{dt} . \end{aligned} \quad (5)$$

This shows that  $J_d(x,t)$  is independent of  $x$  in the region  $0 \leq x \leq s(t)$ .

The displacement current can be related to the potential drop across the sheath,  $V_s$ .

Integrating Eq. (4) one obtains

$$V_s(t) = V(s) - V(0) = -\int_0^s dx' E(x',t) . \quad (6)$$

Differentiating Eq. (6) gives

$$\frac{dV_s}{dt} = -\int_0^s dx' \frac{\partial E(x',t)}{\partial t} - E(s,t) \frac{ds}{dt} . \quad (7)$$

The second term on the right hand side is zero due to Eq. (3), and the integrand is proportional to the displacement current and independent of  $x$ . Thus, one obtains

$$J_d(t) = -\frac{\epsilon_0}{s(t)} \frac{dV_s(t)}{dt} . \quad (8)$$

This result holds for an arbitrary ion density profile, and it is simply the formula for the current flowing across a capacitor, except for the time varying spacing  $s(t)$ . The time dependence of  $s(t)$  generates harmonics in  $J_d$ .

A particularly simple form for the displacement current is in the case of the uniform ion density profile. In this case the potential is quadratic in  $s(t)$  and the displacement current is given by

$$J_d(t) = - \left[ \frac{\epsilon_0 e n_s}{2 V_s(t)} \right]^{1/2} \frac{dV_s}{dt} . \quad (9)$$

The current flowing across the sheath will be approximated by a product of the electrode area,  $A$ , and the current densities in Eqs. (1) and (9). This neglects the effects of two dimensional variation across a single electrode.<sup>28,29</sup> However, this suffices in studying the gross effects of area ratio in asymmetric systems. The area ratio enters into the model equations by equating the current flowing through the A and B sheaths, the two sheaths of the discharge. Using subscripts "A" and "B" to label the various current densities and electrode areas, current continuity is written

$$J_{c,A} + J_{d,A} = - \frac{A_B}{A_A} [J_{c,B} + J_{d,B}] \quad (10)$$

where the expressions for the conduction and displacement current densities are taken from Eqs. (1) and (9). (The minus sign is included on the right side for the B sheath since current is positive if it flows from the plasma to the B electrode.) In asymmetric systems the density at the edges of both sheaths can differ by a factor of 2 to 3 due to ion diffusion in the glow and the mechanism for electron energy deposition.<sup>17,28</sup> However, we note that even larger effects will arise from the sheath density profile,<sup>30</sup> which cannot be treated by the present numerical algorithm; thus, for simplicity we will take the density to be the same at each sheath.

Equation (10) leads to a differential equation which will be integrated numerically. A specific choice for the ion flux is required; we adopt the collisionless presheath result  $u_B = (kT/M_i)^{1/2}$ , where

$M_i$  is the ion mass. Equation (10) is divided by  $(1/4)en_s c_e$ , and is restated in the following dimensionless variables and constants:

$$\begin{aligned}
 U_i &= eV_{s,i}/kT, \quad i=A \text{ or } B \\
 \alpha &= \left[ \frac{2\pi m_e}{M_i} \right]^{1/2} \\
 \beta &= \frac{A_B}{A_A} \\
 \gamma &= \pi^{1/2} \frac{\omega}{\omega_p} \\
 \theta &= \omega t
 \end{aligned} \tag{11}$$

where  $\omega$  is the rf (angular) frequency and  $\omega_p = (n_s e^2 / \epsilon_0 m_e)^{1/2}$  is the plasma frequency. Equation (10) then becomes, for the case of the uniform ion density sheath,

$$-\alpha + \exp(-U_A) - \frac{\gamma}{U_A^{1/2}} \frac{dU_A}{d\theta} = -\beta \left[ -\alpha + \exp(-U_B) - \frac{\gamma}{U_B^{1/2}} \frac{dU_B}{d\theta} \right] \tag{12}$$

The first two terms on each side constitute the conduction current and the third term is the displacement current.

When the B electrode is at ground potential, the voltage applied on the A electrode by the external circuit,  $V_{ext}(t)$ , is given by

$$V_{ext}(t) = -V_{s,A}(t) + V_{s,B}(t) . \tag{13}$$

Assuming that the discharge is driven by a low impedance source, we take  $V_{ext}$  to be the sum of a sine wave plus a dc bias. The dimensionless voltage  $U_{ext} = eV_{ext}/kT$  then has the form

$$U_{ext}(\theta) = -(U_0 + U_1 \cos\theta) \tag{14}$$

where  $U_0$  is the dc bias and  $U_1$  is the rf amplitude. Equation (12) then becomes a first order differential equation in  $U_A(\theta)$  when Eq. (13) is used to eliminate  $U_B$  in terms of  $U_A$  and  $U_{ext}$ :

$$\frac{dU_A}{d\theta} = \frac{\alpha(1+\beta)\exp(-U_A) - \beta\exp(-U_A - U_{ext}) + \beta\gamma(U_A + U_{ext})^{-1/2}U_1\sin\theta}{-\gamma[U_A^{-1/2} + \beta(U_A + U_{ext})^{-1/2}]} \quad (15)$$

The numerical solution of Eq. (15) is nontrivial because the physically desired solution  $U_A(\theta)$  is periodic and yields no dc current upon averaging Eq. (1) over one period (due to the presence of the blocking capacitor  $C_{\text{block}}$  in Figure 1(a)). Two parameters adjusted in the search for the solution are the initial value  $U_A(0)$  and the dc bias  $U_0$ . The algorithm proceeds in the following steps: 1) A guess is made for  $U_0$ ; 2)  $U_A(0)$  is found which belongs to a periodic solution (a fourth-order Runge-Kutta integration scheme is used in this step); 3)  $J_c(\theta)$  is computed and averaged over one period; 4) If the dc current is not below 0.1% of the ion flux, a new  $U_0$  is guessed, and the steps are repeated.

This model is identical to that of Ref. 21, except for the definition of the normalized ion flux  $\alpha$ . In Ref. 21 a factor of 0.606 is included to account for the decrease in density across the presheath. In this work the density is parameterized by its value at the sheath edge instead, as was done in Ref. 16. Other runs, however, have been performed in which the conventions of Ref. 21 were adopted, and it was verified that the algorithm employed in this work does indeed reproduce the sheath voltage data of Ref. 21.

## B. The Single Sheath

In Section III the current obtained from solutions of Eq. (15) will be compared to the current which flows through a single sheath driven with a sinusoidal voltage. The equation for the latter is discussed here for two cases, the first for which the ion density is uniform, and the second for which it is a particular nonuniform density profile.

In the uniform density case, the left side of Eq. (12) still describes the current density, but now  $U_A$  is given the form of  $U_{ext}$  in Eq. (14). Upon requiring the conduction current to average to zero over one period, one obtains

$$U_0 = \ln(I_0(U_1)) + \frac{1}{2} \ln\left(\frac{M_i}{2\pi m_e}\right) \quad (16)$$

where  $I_0$  is the modified Bessel function of zero order. The second term is the floating potential in the absence of oscillations in the sheath voltage. Ion creation and transport processes can change the numerical coefficients of the normalized fluxes in the expression for the conduction current,<sup>25,26,31,32,33</sup> and hence  $U_0$ , but these effects will not change the conclusions to be obtained for the current waveforms.

The sheath ion density may be fairly uniform when ion motion through the sheath is highly collisional.<sup>34,35,36,37</sup> However, at lower pressures there will be a drop in the ion density in the direction from the plasma to the electrode due to the acceleration of ions through the sheath potential (see Figure 1(b)). One consequence of this is that the maximum sheath thickness will be larger. Thus, the displacement current density, given by Eq. (8), will be reduced. This motivates a study of the displacement current waveform when the sheath ion density is nonuniform. This will lead to a more complicated numerical problem for two sheaths which we do not solve here. However, we will later show how this case can be approximated by the uniform density case with an adjustment of parameters, and the effect of a two sheath system on the current waveform will be seen to be even more striking in this case.

To this end, we present a model for the displacement current flowing through a single sheath with a nonuniform ion density profile. The desired result is an expression for  $s(t)$  in Eq. (8) in terms of the sheath voltage  $V_s$ . A self-consistent ion density profile will not be used, but instead the ion density profile from a Child law sheath<sup>38</sup> will be used. The advantage of these simplifications is that it allows a closed form expression for computation of  $s(t)$ . (Van Roosmalen and Van Voorst Vader<sup>39</sup> have used a similar idea, and had to divide the rf period into anodic and cathodic parts in order to assure that the time-averaged sheath potential was in fact the potential accelerating the ions. This, however, results in some mathematical complexity which is not necessary if one wants only an estimate of the effects of density inhomogeneity.) The ion density in the coordinate system of

Figure 1 is

$$n_i(x) = \left[ \frac{2 \epsilon_0 M_i}{9 e^2} (n_s u_B)^2 \right]^{1/3} (x_m - x)^{-2/3} . \quad (17)$$

This is obtained from conservation of ion flux and ion energy. The initial ion speed at the maximum sheath position  $x = x_m$  was neglected in Eq. (17), and thus  $n_i$  diverges at  $x = x_m$ . But  $ds/dt$  vanishes at that point, so that the displacement current as expressed in Eq. (5) also vanishes at the extreme sheath edge position. As the sheath edge  $s(t)$  moves between  $x=0$  and  $x=x_m$ , Poisson's equation and Eq. (3) give the sheath voltage drop  $V_s(t)$ . This is written using the variable  $q \equiv 1 - s(t)/x_m$  as

$$V_s(t)/V_m = 1 - (4/3)q^{1/3} + (1/3)q^{4/3} \quad (18)$$

where  $V_m$  is the maximum sheath voltage occurring when  $s(t) = x_m$ . This is a quartic in the variable  $w \equiv q^{1/3}$  and must be inverted to find  $s(t)$ . Standard formulae provide the solution:<sup>40</sup>

$$y \equiv 4(g/3)^{1/2} \cosh \left[ (1/3) \cosh^{-1} \left( (3/g)^{3/2} \right) \right] \quad (19)$$

$$w = y^{1/2}/2 - \left[ 2/y^{1/2} - y/4 \right]^{1/2} .$$

where  $g \equiv 3(1 - V_s(t)/V_m)$ . The sheath edge is finally obtained from

$$s(t) = x_m [1 - w^3(t)] . \quad (20)$$

In the nonuniform density model the maximum sheath voltage enters the solution  $s(t)$ . This additional complication is absent in the uniform density model.

Equations (1) and (8) give the displacement and conduction currents, respectively. The sheath voltage  $U \equiv eV_s/kT$  is given the form of  $U_{\text{ext}}$  in Eq. (14), and the total current is nondimensionalized by dividing by  $(1/4)en_s c_e$ . The total current  $J_T(\theta)$  is

$$J_T(\theta) = -\alpha + \exp(-U) + \frac{\gamma_2 U_1 \sin \theta}{(U_0 + U_1)^{3/4} (s/x_m)} \quad (21)$$

where  $\gamma_2 = 3\pi^{(1/2)} 2^{(-3/4)} \omega/\omega_p$ , and  $s/\kappa_m$  is obtained directly from Eq. (20).

### III. Results and Discussion

Discharge current waveforms obtained from the solution to Eq. (15) are presented in this section. Voltage and current are specified in dimensionless values, the voltage being in units of  $kT/e$  and the current density being in units of  $(1/4)n_s c_e$ . The rf frequency used is 10 Mhz, and the ion mass in  $u_B$  is 40 amu, unless otherwise noted.

#### A. Current Waveforms

Figure 2 shows current waveforms for  $U_1 = 300$ ,  $n_s = 10^{10} \text{ cm}^{-3}$ , and area ratio  $\beta = 1, 2.1,$  and 4. (The combination of  $U_1$  and  $n_s$  was chosen from our experiments on 70 mtorr argon discharges.) Also plotted is the (uniform density) single sheath limit current waveform. This series of waveforms shows that the current waveforms approach the single sheath limit as the area ratio is increased; the waveforms become more skewed due to the  $[s(t)]^{-1}$  dependence in Eq. (8), and the conduction current spike visible in the single sheath limit at  $180^\circ$  is just forming at  $\beta \sim 4$ . Other runs showed that the spike emerges as distinct between an area ratio of 5 and 6. However, at a lower rf amplitude of 30, and a corresponding lower density parameter of  $10^9 \text{ cm}^{-3}$ , the conduction current spike did not appear as a distinct feature of the total current waveform even in the single sheath limit.

The changing skewness of the current waveforms implies greater harmonic content as the area ratio increases above unity. In Figure 3 this is shown more directly by plotting the frequency spectra for the total current (a), and the conduction current (b), at sheath A for  $U_1 = 300$ ,  $n_s = 10^{10} \text{ cm}^{-3}$ , and area ratios of 1, 2.1, and 8. The spectra are normalized to the first harmonic. There is hardly any higher harmonic current content for area ratio  $\beta = 1$ ; the minute higher harmonic amplitude that does exist is due to the inclusion of the conduction current, absent in the treatment of Ref. 15. However, at an area ratio of 2.1 the amplitude of the third harmonic is still ~10% of the first harmonic; and for an area ratio of 8, the fifth harmonic is still ~10% of the first harmonic. This is

consistent with the experimental observation that symmetric systems have simpler impedance characteristics.<sup>41</sup> In Figure 3(b) the conduction current frequency spectrum broadens as area ratio increases since the conduction current pulse becomes narrower and larger in height.<sup>26</sup> For example, at  $\beta = 1$  the first harmonic displacement current amplitude was -0.32 and the conduction current peak height was -0.1, whereas at  $\beta = 8$  the displacement current amplitude was -0.41 and the conduction current peak height was -0.32.

### B. Effect of Large $n_s$ .

Equation (8) shows that the displacement current varies as the inverse of the sheath thickness. A rough estimate for the ratio of the displacement currents in the uniform density and Child law sheath models is given by the ratio of the maximum sheath thicknesses:

$$\frac{J_{d,uniform}}{J_{d,C.L.}} = \frac{x_{m,C.L.}}{x_{m,uniform}} = \frac{2^{3/4}}{3} \left( \frac{eV_m}{kT} \right)^{1/4} \quad (22)$$

For  $eV_m/kT = 300$ , this ratio is -3, thus the uniform sheath model allows too large a displacement current. We next study the consequences of reducing the displacement current within the framework of the uniform density model.

Figure 4(a) shows the current waveforms from the single sheath model with nonuniform density. The rf amplitude  $U_1$  is 300 and the density is  $10^{10} \text{ cm}^{-3}$ . The displacement current waveform shown here is similar to Biehler's results from a self-consistent solution to Poisson's equation in the sheath for a xenon rf discharge.<sup>27</sup> (The peak displacement current in Figure 4(a) is only about 25% lower than that estimated from Fig. 3 of Ref. 27.) The peak value for the displacement current here is -0.1 compared with the peak value -0.5 for the single sheath, uniform density case shown in Figure 2. The reduction in the displacement current is even greater than the estimate obtained from Eq. (22). In Eq. (1) the conduction current depends only on the sheath voltage, so that with a

reduced displacement current, the conduction current spike is more prominent.

We now consider how the mutual interaction of two sheaths affect the current waveform. The difference between the waveforms in Figure 4(a) and Figure 2 is the relative size of the displacement to the conduction current. Therefore, the effect of two interacting sheaths on the impedance of the discharge may be investigated with the uniform ion density sheath model by finding a case for which the relative sizes of the displacement and conduction currents are similar to the waveforms in Figure 4(a). Such a case can be devised by adjusting the density parameter in the expression for the displacement current:  $\gamma$  varies as  $n_s^{-1/2}$ . An example of this is shown in Figure 4(b); this is a result of the single sheath model, with a uniform density sheath, where the rf voltage  $U_1$  is 300 and the density parameter is  $23 \times 10^{10} \text{ cm}^{-3}$ . The density is unrealistically large, but the current waveform is similar to the case shown in Figure 4(a). In this sense, the relative size of the displacement to the conduction currents is more appropriate.

Figure 5 shows the current waveforms from the two sheath model for an area ratio of 2.1, and the same  $n_s$  and  $U_1$  as the example in Figure 4(b). The large conduction current spike of Figure 4(b) is less obvious in Figure 5. This is because the sheath voltage  $U_A(\theta)$  is flattened near its minimum, broadening the conduction current pulse at sheath A. (The maximum voltage  $U_A$  was reduced to -250 due to the voltage division between the two sheaths, but this by itself has only a small effect in reducing the conduction current spike.)

The smoothing is even more dramatic for the symmetric discharge. Figure 6 shows the sheath voltage and current waveforms for  $\beta = 1$ , and  $n_s$  and  $U_1$  as in Figure 5. The sheath voltage in Figure 6(a) has a broadened minimum and the minimum sheath voltage occurs before  $180^\circ$ . In part Figure 6(b) the peak in the conduction current has moved toward the peak in the displacement current, which decreases suddenly due to the flattening of the sheath voltage waveform as the conduction current rises. The end result is that the total current does not show the distinct conduction current pulse at  $180^\circ$  which appears in the single sheath limit. Also note that near  $150^\circ$  the discharge current changes from mostly conduction current at sheath A to predominantly

displacement current at sheath B.

#### IV. Comparison to Other Works

The two-coupled sheath model presented here is highly simplified. Our intent is to develop qualitative understanding of the features appearing in current waveforms measured in experiments. Still, it is important to see how the results presented here relate to results from more sophisticated, self-consistent models. There are several examples of current waveforms to be found in the literature on rf discharge modeling and experiment.

Figure 6 showed the voltage and current waveforms for a symmetric voltage-driven discharge. The sheath voltage displays a broad low voltage region and the minimum sheath voltage occurs before the extreme value of the external voltage. This has been observed in several simulations.<sup>42,43,44,45,46</sup> Figure 10 of Ref. 44 presents an especially interesting comparison between the current waveforms for the wave-riding and secondary electron regimes in a helium discharge, which serves to illustrate the sensitivity of the current waveforms to the relative sizes of the conduction and displacement currents, as indicated by the two sheath model. The frequency was 3.2 MHz and the gas pressure was 3 torr. In the wave-riding regime ionization is dominated by electrons which are ohmically heated at the sheath-glow interface, and the steady-state plasma density varied from  $2 \times 10^8 \text{ cm}^{-3}$  to  $10^9 \text{ cm}^{-3}$  as the rf amplitude increased from 100 to 250 V. The current waveforms for an rf amplitude of 120 V in Fig. 10(a) of Ref. 44 show that the peak conduction current is only ~14% of the peak displacement current, and that the conduction current appears as a fairly symmetrical pulse-like perturbation on the total current. This is similar to the unity area ratio curve in Figure 2, where the conduction current (not shown) is a small, fairly symmetrical pulse near the zero crossing of the total current. The interesting effect occurs in Ref. 44 when the rf amplitude is increased above 250 V and the secondary electron regime is entered. In this regime secondary electrons dominate the total ionization and by virtue of the large amount of energy acquired by each secondary electron as it crosses the sheath, the plasma density increases to  $10^{12} \text{ cm}^{-3}$  at an rf

amplitude of 400 V. This corresponds to a smaller  $\gamma$  in Eq. (12) of the two-sheath model. Figure 10(b) of Ref. 44 shows that the electron conduction current waveform is broader and more skewed, with its peak being shifted backwards in phase. This is similar to the conduction current curve  $J_c$  in Figure 6. One result of the two-sheath model is that the current waveforms depend on the relative sizes of the conduction and displacement currents. In the simulation of Ref. 44 this is influenced by the transition between the wave-riding and secondary electron regimes, and one finds that the current waveforms in each regime show the qualitative features predicted by the two-sheath model for small and large conduction current components.

The applicability of the two-sheath model to the results of Ref. 44 may be questioned due to the low frequency (3.2 MHz) used in Ref. 44. At a few MHz, simulations show that the ion flux is strongly modulated,<sup>42,43,44</sup> contrary to what is assumed by Eq. (1). The total current shown for the secondary electron regime in Ref. 44 is roughly sinusoidal with flat, slanted peaks. This waveform has been observed by Hebner and Verdeyen<sup>47</sup> for a helium discharge at 500 mtorr and 2.6 MHz. The two-sheath model with uniform density sheaths instead produces a sawtooth wave, a typical example of which is given in Figure 7. It is not clear if this difference is due to an incorrect sheath density profile (for the displacement current), an incorrect ion flux, or some other factor. The correct ion flux may not be so important; Fig. 6 of Ref. 42 showed PIC simulation current waveforms for a symmetric 1.5 MHz, 350 mtorr, 500 V, voltage-driven helium discharge. The total current was also a triangular wave with a peak magnitude of  $\sim 6 \text{ A/m}^2$ . For that example, the glow density was  $\sim 3 \times 10^{15} \text{ cm}^{-3}$ , and the density was not strongly attenuated in the sheath. Using the parameter values given above, and estimating  $T_e$  to be  $\sim 2 \text{ eV}$ , the two-sheath model gives the waveform in Figure 7. The dimensionless current density of 0.1 corresponds to  $\sim 11 \text{ A/m}^2$ , just a factor of two greater than the simulation result.

There are also some interesting experimental results by Horwitz and Puzzer<sup>48</sup> on the effects of area ratio on the conduction waveforms. Their experimental system consisted of an argon discharge driven at 13.56 MHz in a chamber of variable target to wall area ratio. The wall electrode in their

system was powered, so that a gridded particle collector could be installed on the target electrode. In Fig. 9 of Ref. 48 are shown conduction current waveforms for area ratios of 0.87 and 10. At a pressure of 3.7 Pa (28 mtorr) the conduction current for the .87 area ratio is broad and occurs before the conduction current pulse for the  $\beta=10$  case. This is similar to Figure 6. When the area ratio is 10, the conduction current peak is narrower. Fig. 10 in Ref. 48 shows that at 21 Pa (158 mtorr) the conduction current waveforms are both narrow pulses. In the two-sheath model the conduction current is always pulse-like for  $\beta = 10$ , simply because it is so close to the single sheath limit. The conduction current for  $\beta = 0.87$  is more interesting, and within the framework of the two-sheath model, the transformation from a broad to narrow pulse suggests a transition to a more uniform ion density sheath with increasing pressure. There is some experimental evidence that the sheath density inhomogeneity is decreased in this higher pressure range.<sup>35,37</sup>

## V. Features of Experimental Data

One motivation for this model was to understand current waveforms we have measured in connection with power measurements in rf discharges. In this section the two-sheath model results will be compared to experimental waveforms we have obtained.

Figure 8(a) shows a current waveform obtained from an argon discharge confined within a cylindrical cavity 9 inches in diameter and 2.5 inches in height. One flat side of the cavity is the powered electrode and the remaining surfaces compose the grounded electrode. The geometrical area ratio is approximately 2.1. For the waveform shown, the gas pressure was 70 mtorr and the voltage at the powered electrode was approximately 700V in amplitude (there was some distortion, as shown by the scaled voltage waveform  $V/350$ ). A sixth harmonic ripple is visible, and this persists to some extent at lower voltages and other pressures. We believe this is due to the frequency response of the external circuit. Figure 8(b) shows the Fourier amplitudes of the waveform in part (a). There is a sharp attenuation of harmonics beyond the sixth, and this is partly responsible for the visible ripple in part (a).

Two features may be noted in the experimental waveform. First, it is nearly an odd function with respect to a zero crossing. Secondly, the waveform is skewed, similar to the model results in Figure 2 or Figure 5. This skewness disqualifies this waveform as one from a symmetric discharge where the symmetry  $I(\theta) = -I(\theta-\pi)$  is observed. (This is equivalent to no even harmonics, contrary to the spectrum in Figure 8.)

The near odd symmetry with respect to a zero crossing is relevant to the two-sheath model. Figure 9 shows two waveforms: (1) The two-sheath model current resulting from a sinusoidal external voltage, and (2) the waveform arising when the voltage waveform measured from the experiment is used for  $V_{\text{ext}}(t)$  and the resulting current is truncated at the sixth harmonic. (The experimental voltage waveform is shown in Figure 8(a) and exhibits a flattened positive half-cycle.) The waveform induced by the sine wave external voltage shows a small, but sharp conduction current spike. This is reduced somewhat when the external voltage waveform is used, but is still visible. However, the waveform with the truncated spectrum shows no spike and its symmetry is greater. (The current waveform without truncation follows the truncated waveform, except at the current spike. Also, when the current arising from the sine wave voltage is truncated, the result still exhibits noticeable asymmetry.)

The experimental waveform and two-sheath model result cannot be expected to match each other precisely due to the models employed for the displacement current and sheath density profile, and also the neglect of the external circuit. However, this comparison illustrates how experimental waveforms may be better understood, and further clarifies how the external circuit manifests itself, namely in its response to higher harmonics and in the voltage distortion it exhibits. There has been some simulation work on symmetric discharges and asymmetric discharges with external circuits.<sup>46,49</sup> From this simple two-sheath model, one can learn the following: 1) If the voltage across an asymmetric discharge is large and sinusoidal, then the current will be non-sinusoidal and can exhibit conduction current spikes and asymmetry with respect to zero crossings. 2) If distortion in the voltage is allowed, then the spikes can be reduced to some degree. Also, because the asymmetry is contained

in the higher harmonics, the actual observation of such asymmetry at low area ratio would require uncommon control of the frequency response of the external circuit.

## VI. Relation to the Pure Resistive Model

Versions of Eq. (10) have been studied previously by workers interested in describing the time-averaged sheath voltage.<sup>16,17,18,19,20,21</sup> The treatment in Ref. 16 is interesting because it neglects the capacitive current ( $\gamma = 0$ ) and yet produces quite good agreement with measurements of the time-averaged sheath potential in symmetric discharges. In this section we compare some sheath voltage results from the pure resistive model (the "R model") to those from the resistive-capacitive model (the "RC model"), that is, Eq. (12) with  $\gamma \neq 0$ .

Figure 10 shows a plot of the dc bias  $U_0$  over a wide range of rf amplitude  $U_1$ . The lower two curves, A and B, are for an area ratio  $\beta = 2.1$ . Curve A is from the RC model with  $n_s = 10^9 \text{ cm}^{-3}$  and  $\omega/2\pi = 10 \text{ MHz}$ ; for  $10^9 \text{ cm}^{-3} < n_s < 10^{10} \text{ cm}^{-3}$  (that is,  $0.02 < \gamma < 0.06$ ) curve A shifts by less than 10% over the entire range of  $U_1$  shown, and shifts by less than 5% for  $U_1 > 40$ . Curve B is from the R model. In the R model the external voltage is divided between the two sheaths by the nonlinear sheath resistances. In the RC model the sheaths are predominantly capacitive (phase shifts of the current to voltage are just a few degrees less than  $90^\circ$  for the first harmonic) and the voltage division is determined by these nonlinear capacitors. Despite this difference, the dc bias produced by both models are quite close, and differ for  $\beta = 2.1$  by less than 20%. In Appendix A it is shown that curves for all values of  $\gamma$  at a given area ratio should converge for small  $U_1$  when the densities at both sheath edges are the same. It is interesting that the results for the R and RC models remain close at large  $U_1$ .

A comparison between the R model and the purely capacitive sheath model provides some understanding of why the dc bias for the R and RC models are similar at large  $U_1$ . Meijer and Goedheer<sup>21</sup> have used this two-sheath model to study the sheath voltages and dc bias. For the purely capacitive sheath (Eq. (10) with the conduction currents neglected) they have shown (in the present

notation) that  $U_0 = U_1(\beta^2-1)/(\beta^2+1)$ . At large  $U_1$  this is close to the R model result. For example, this is only 30% larger than the R model curve for  $U_1 > 20$  at  $\beta = 2.1$ . Thus, although the current and the sheath voltage differ in the two cases of the purely resistive and the purely capacitive sheath models, current continuity forces both systems to develop similar dc biases at large rf amplitudes.

The dc bias for both R and RC models is even closer at  $\beta = 10$ ; curve C is the result from the RC model for  $n_s = 10^9 \text{ cm}^{-3}$ , but the result for  $n_s = 10^9 \text{ cm}^{-3}$  and the R model differ from curve C by less than 5%. In some sense, at larger area ratio all such curves are constrained by the topmost curve (labeled D) showing the single sheath limit:  $\ln(I_0(U_1))$ .<sup>16</sup> Note that since the curves for smaller  $\beta$  follow the single sheath limit, curve D, the dc bias plotted against the rf amplitude (at large rf amplitude) should extrapolate to a point below the origin at  $U_1=0$ , as shown by Köhler et al..<sup>24</sup> Note also that the ratio of the dc bias to the rf amplitude decreases with rf amplitude (at a given area ratio), as shown by the data of Horwitz.<sup>50</sup>

Figure 10 suggests that the R model reproduces the sheath voltages quite well. This is explored further in Figure 11. Figure 11(a) shows the ratio of the time-averaged sheath voltages  $U_A^{(0)}/U_B^{(0)}$  (the "dc voltage ratio"). Figure 11(b) shows the ratio of the first harmonic amplitudes of the sheath voltages  $U_A^{(1)}/U_B^{(1)}$  (the "rf voltage ratio"). The R model results for rf amplitudes  $U_1$  of 300 and 30 appear as curves B and D, respectively. The corresponding RC model results (curves A and C) are shown only for  $n_s = 10^9 \text{ cm}^{-3}$ ; the plots are not very sensitive to  $n_s$  on a logarithmic scale. The straight dashed line with a slope of two represents the  $\beta^2$  scaling which results from capacitively conducted currents through two uniform ion density sheaths of equal densities.<sup>51</sup> (One can show that the  $\beta^2$  scaling is only true for area ratios greater than  $\sim 3$ , even for this ideal case; the  $\beta^2$  line is plotted only for reference.) The curves of Figure 11(a) all have the same general form, exhibiting saturation at large  $\beta$  to the value  $U_0$  in Eq. (16) divided by the dc floating potential (the second term in Eq. (16)).<sup>16,28</sup> The R and RC models are both sensitive to the value of the rf amplitude; as  $U_1$  decreases, the dc voltage ratio increases more slowly with area ratio  $\beta$ . In Appendix B the R model is studied further and it is shown that the correction to the exponent of 2 in the  $\beta^2$

scaling is roughly a factor equal to the ratio of the dc floating potential to the time-averaged sheath voltage at  $\beta = 1$ .

However, the behavior of the rf voltage ratio in the R and RC models differ. Figure 11(b) shows that this ratio is sensitive to  $U_1$  in the RC model, but that it maintains a  $\beta^2$  variation (for  $\beta$  close to 1) in the R model for a wide range of  $U_1$  from 300 to 30 (as shown), and even smaller. In Appendix B the R model is examined further and it is shown that the correction to the exponent of 2 in the  $\beta^2$  scaling (at  $\beta$  close to 1) is of order  $(1/U_1)^2$  and does not involve the dc floating potential. This is indicative of the nearly invariant sheath voltage waveforms in the R model: They are rectified parts of the external voltage. In fact, the  $\beta^2$  scaling (to zero order in  $1/U_1$ ) can be simply derived from this observation. However, in the RC model there is a coupling between the conduction and displacement currents that causes the sheath voltage waveforms to vary with  $U_1$ , and this is responsible for the variation in the rf voltage ratio with  $U_1$ .

Regarding current waveforms, the R model cannot be expected to give good current waveforms since the capacitive current has been omitted. Additionally, since the coupling between the capacitive and displacement currents is omitted, broadening and skewing of the electron conduction current pulse is not produced by this model, nor is the conversion of conduction current at one sheath to displacement current at the opposite sheath possible in this model.

## VII. Summary

In this paper we have presented a simple model to describe the conduction of current through an asymmetric parallel plate rf discharge. In order to make this as computationally simple as possible, a uniform ion density in the sheaths was assumed.

The model suggests the following for current waveforms:

- 1) In the limit of large area ratio, the discharge current approaches that of the single sheath, and consequently the harmonic content in the current increases. Also, for a uniform ion density sheath discharge driven at a fairly high voltage, the conduction current spike is noticeable for area ratios as

low as 6. In a nonuniform ion density sheath model this property of the single sheath limit would persist to even lower area ratios.

2) An example was given in which the peak magnitudes of the conduction and displacement currents are chosen to model those expected in a Child law sheath. It was found that at moderate area ratio, both sheath voltages are appreciable in magnitude and exhibit distortions that broaden the electron current pulse. The sheath voltage minimum is also moved backward in phase, and this allows the electron current pulse to merge with the displacement current. The net result is the suppression of the distinct electron pulse evident in the single sheath limit. In the symmetric discharge these effects are most complete, and fairly sinusoidal current waveforms can be maintained even with a very large conduction current component.

Examples from simulations and experiment were presented to show that qualitative features of the current waveforms resulting from the two-sheath model are not unrealistic. In particular, current waveform examples are cited from simulation and experiment that may be interpreted in terms of the sensitivity of the total current waveform to the relative sizes of the conduction and displacement currents, and the sheath ion density profile.

An example from our own experiments was given in which the current smoothing property demonstrated by the two-coupled-sheath system is important in describing the measured current waveform. We find that the external circuit response to the discharge current load is also important in determining the final current waveform.

The pure resistive limit to the model was examined further since previous workers established that such a model could predict the time-averaged sheath voltage. It was found that such a model is not able to reproduce some of the properties of the rf component of the sheath voltage which depend on the coupling between the conduction and displacement currents.

#### ACKNOWLEDGMENT

This work was supported by NSF Grant ECS-8517363 and DOE Grant DE-FG03-87ER13727.

APPENDIX A: Small Signal Treatment of  $U_0$  vs.  $U_1$

The dc bias is studied at small rf amplitude in this appendix. Equation (12) is linearized by writing

$$U_i = U_f + \delta U_{dc,i} + \delta U_{rf,i}(\theta) \quad , i = A \text{ or } B \quad (\text{A1})$$

where  $U_f$  is the dc floating potential, and  $\delta U$ 's are the dc and rf first order corrections to  $U_i$  when the perturbation  $-U_1 \cos\theta$  is applied between electrodes A and B. Averaging Eq. (12) over one period and setting the average current to zero gives the standard result that  $\delta U_{dc,i} = \ln(I_0(\delta U_{rf,i}))$ . (The argument of the modified Bessel function is now the amplitude of  $\delta U_{rf,i}(\theta)$ .) Expanding this relation shows that  $\delta U_{dc,i}$  is second order in the perturbation amplitude:

$$\delta U_{dc,i} = \delta U_{rf,i}^2/4 + \mathcal{O}(4) \quad (\text{A2})$$

where the second term on the right side represents fourth order terms in the perturbation. Thus, to first order, the correction to  $U_i$  is simply  $\delta U_{rf,i}$ ; there is no first order dc correction.

Equation (12) is linearized to give the small signal circuit model of the two-sheath system. After Fourier transforming, one obtains

$$(G_A + iB_A)(-\delta U_{rf,A}) = \beta (G_B + iB_B)\delta U_{rf,B} \quad (\text{A3})$$

where  $G_A = G_B = \exp(-U_f)$  and  $B_A = B_B = \gamma/U_f^{1/2}$  are the conductances and susceptances for a unit area. The minus sign appearing with  $\delta U_{rf,A}$  is due to the polarity implied by Eq. (13). The admittances  $Y_A = G_A + iB_A$  and  $Y_B = \beta(G_B + iB_B)$  may be identified in Eq. (A3). When the sheath densities  $n_{s,A}$  and  $n_{s,B}$  are the same,  $Y_B = \beta Y_A$ , and the two sheaths act as a voltage divider with constant gain and no phase shift. One then obtains

$$\begin{aligned} -\delta U_{rf,A} &= (-U_1) \beta / (\beta + 1) \\ \delta U_{rf,B} &= (-U_1) / (\beta + 1) \end{aligned} \quad (\text{A4})$$

Equation (13) gives the dc bias as  $-\delta U_{dc,A} + \delta U_{dc,B}$ . Upon using Eqs. (A2) and (A4), one obtains

$$U_0 = -\frac{1}{4} \frac{\beta - 1}{\beta + 1} U_1^2 + \mathcal{O}(4) , \quad (\text{A5})$$

In Ref. 16 it was found at large  $U_1$  that  $U_0$  fitted the curve  $(1-\beta^{-1})\ln( I_0(U_1) )$  quite well. This is a faster dependence on  $\beta$  than shown in Eq. (A5), but is consistent with the spacing of the curves in Figure 10 at small and large  $U_1$ .

When  $n_{s,A} \neq n_{s,B}$ ,  $\beta$  appearing in Eq. (12) becomes  $\beta' = (A_B n_{s,B}) / (A_A n_{s,A})$ , and in Eq. (A4)  $\beta$  is replaced by  $\zeta = Y_B / Y_A = \beta' (G_B + iB_B) / (G_A + iB_A)$ . The electrons are still assumed to be isothermal, so  $G_A = G_B$ . But now using Eq. (8) and normalizing by the random electron flux,  $B_i \propto (n_{s,i} s_i)^{-1}$ , we find  $B_A \neq B_B$ . For a given floating potential, the sheath thickness will also vary with the density. Thus  $\zeta$  is a complex number and exhibits a dependence on the density ratio in  $\beta'$  and the ratio of the susceptances.  $U_0$  is given by

$$U_0 = -\frac{1}{4} U_1^2 \frac{|\zeta|^2 - 1}{|\zeta + 1|^2} + \mathcal{O}(4) \quad (\text{A6})$$

and also will depend upon the density ratio. The two curves for an area ratio of 2.1 in Figure 10 should then separate at low  $U_1$ .

Appendix B: Pure Resistive Model Near  $\beta = 1$ .

In this appendix the voltage ratios for the pure resistive model shown in Figure 11 are studied for area ratios slightly above unity. Godyak and Kuzovnikov<sup>16</sup> solved Eq. (12) with  $\gamma = 0$ ; analytical expressions for  $U_A$  and  $U_B$  were derived. They obtained (in the present notation and conventions)

$$U_A(\theta) = \ln \left\{ \frac{1 + \beta \exp(-U_{\text{ext}})}{\alpha (1 + \beta)} \right\} \quad (\text{B1})$$

Let  $f(\theta) = U_A$  for  $\beta = 1$ . Consider now the perturbed system in which the area ratio is slightly above unity:

$$\begin{aligned} \beta &= 1 + \epsilon, \quad \epsilon \ll 1 \\ U_A &= f + \delta U_A \\ U_{\text{ext}} &= -U_0 - U_1 \cos \theta \end{aligned} \quad (\text{B2})$$

$U_0$  is the first order correction to the external voltage. Expanding Eq. (B1) gives

$$\delta U_A = U_0/2 + (\epsilon + U_0)(1 - \exp(-f)/\alpha)/2 \quad (\text{B3})$$

Note that since  $\langle \exp(-f) \rangle = \alpha$ ,  $\langle \delta U_A \rangle = U_0/2$ . (The brackets denote averaged values.) Equation (13) gives the correction to  $U_B$  as  $\delta U_B = -U_0 + \delta U_A$ . The dc bias  $U_0$  is obtained by setting the average conduction current to zero. At first order one obtains  $\langle \exp(-f) \delta U_A \rangle = 0$ , and this implies that

$$\begin{aligned} U_0 &= \epsilon C / (1 - C) \\ \text{where } C &= \langle \exp(-2f) \rangle / \alpha^2 - 1 \end{aligned} \quad (\text{B4})$$

The function  $\exp(-f)$  resembles a square pulse for large  $U_1$ ; and as  $U_1$  approaches infinity,  $C$  approaches unity. The integral in Eq. (B4) was done numerically:

$$C = 1 - 4/(\pi U_1) \quad (\text{B5})$$

The first order term is good to three digits for  $80 < U_1 < 300$ , and at  $U_1 = 10$  the correction is -2%.

The voltage ratios are to first order

$$\begin{aligned}\frac{U_A^{(0)}}{U_B^{(0)}} &= 1 + \frac{U_0}{\langle f \rangle} \\ \frac{U_A^{(1)}}{U_B^{(1)}} &= 1 + 2 \frac{\delta U_A^{(1)}}{f^{(1)}}.\end{aligned}\tag{B6}$$

(The superscripts denote the dc and first harmonic amplitudes.) Note that a quadratic variation in area ratio would make the right side of these expressions  $1 + 2\epsilon$ . The Fourier amplitudes are obtained from Eq. (B1) (for  $\beta = 1$ ) and Eq. (B3). The integral for  $f^{(1)}$  can be done, and gives  $f^{(1)} = U_1/2$ . The integrals for  $\langle f \rangle$  and  $\delta U_A^{(1)}$  were partly done numerically:

$$\begin{aligned}\langle f \rangle &= \frac{U_1}{\pi} + \ln \left( \frac{1 + \exp(-U_1)}{2\alpha} \right) + \frac{1.665}{\pi U_1^2} \\ \delta U_A^{(1)} &= \frac{2}{\pi} (\epsilon + U_0) \left( 1 - \frac{1.647}{U_1^2} \right)\end{aligned}\tag{B7}$$

(For  $100 < U_1 < 300$  the second order terms are accurate to at least three digits, and at  $U_1 = 10$  the correction is less than -4%.) Thus, the voltage ratios are to good approximation

$$\begin{aligned}\frac{U_A^{(0)}}{U_B^{(0)}} &= 1 + \epsilon \frac{\pi^2}{4} \frac{(1 - 4/(\pi U_1))}{(1 - (\pi/U_1) \ln(2\alpha))} \\ \frac{U_A^{(1)}}{U_B^{(1)}} &= 1 + 2\epsilon \left( 1 - \frac{1.647}{U_1^2} \right).\end{aligned}\tag{B8}$$

Thus, for large  $U_1$  the dc voltage ratio scales as a power of  $\beta$  with a maximum exponent of -2.47. Also, the term involving the logarithm in the denominator is roughly the dc floating potential divided by  $\langle f \rangle$ , and can be significant when the rf amplitude is as high as a few tens of  $kT/e$ .

The quadratic scaling for the rf amplitude ratio does not hold for all  $U_1$ . For example, one can show from Eq. (B1) that at small  $U_1$  (to first order)

$$\begin{aligned}
 C &= 0 \\
 f &= \frac{U_1}{2} \cos\theta - \ln\alpha \\
 \delta U_A^{(1)} &= \epsilon \frac{U_1}{4}
 \end{aligned}
 \tag{B9}$$

and hence,

$$\begin{aligned}
 \frac{U_A^{(0)}}{U_B^{(0)}} &= 1 \\
 \frac{U_A^{(1)}}{U_B^{(1)}} &= 1 + \epsilon
 \end{aligned}
 \tag{B10}$$

Thus for small  $U_1$  and  $\beta$  close to 1, the rf voltage ratio will scale linearly with  $\beta$ , and the dc voltage ratio will depend on a higher order term in  $U_1$ .

## REFERENCES

1. J.S. Logan, N.M. Mazza, and P.D. Davidse, *J. Vac. Sci. Technol.* **6**, 120 (1969).
2. K. Ukai and K. Hanazawa, *J. Vac. Sci. Technol.* **16**, 385 (1979).
3. D. B. Ilić, *Rev. Sci. Instrum.* **52**, 1542 (1981).
4. A.J. van Roosmalen, *Appl. Phys. Lett.* **42**, 416 (1983).
5. C. Beneking, *J. Appl. Phys.* **68**, 4461 (1990).
6. J.W. Butterbaugh, L.D. Baston, and H.H. Sawin, *J. Vac. Sci. Technol. A* **8**, 916 (1990).
7. W.G.M. van den Hoek, C.A.M. de Vries, and M.G.M. Heijman, *J. Vac. Sci. Technol. B* **5**, 647 (1987).
8. C.M. Horwitz, *J. Vac. Sci. Technol. A* **1**, 1795 (1983).
9. S.E. Savas, D.E. Horne, and R.W. Sadowski, *Rev. Sci. Instrum.* **57**, 1248 (1986).
10. V.A. Godyak and R.B. Piejak, *J. Vac. Sci. Technol. A* **8**, 3833 (1990).
11. V.M. Donnelly, D.L. Flamm, G. Collins, *J. Vac. Sci. Technol.* **21**, 817 (1982).
12. K.E. Greenberg, P.J. Hargis, and P.A. Miller, Sandia National Laboratories internal report SETEC 90-013, Nov. 1990.
13. F. Tochikubo, T. Kokubo, S. Kakuta, A. Suzuki, and T. Makabe, *J. Phys. D. (UK)* **23**, 1185 (1990).
14. M.A. Lieberman, *IEEE Trans. Plasma Sci.* **16**, 638 (1988).
15. V.A. Godyak, *Sov. J. Plasma Phys.* **2**, 78 (1976).
16. V.A. Godyak and A.A. Kuzovnikov, *Sov. J. Plasma Phys.* **1**, 276 (1975).
17. S.E. Savas, *Mat. Res. Soc. Symp. Proc.* **98**, 35 (1987).
18. A.M. Pointu, *Appl. Phys. Lett.* **50**, 1047 (1987).
19. A.M. Pointu, *J. Appl. Phys.* **60**, 4113 (1986).
20. P.M. Vallinga and F.J. de Hoog, *J. Phys. D* **22**, 925 (1989).
21. P.M. Meijer and W.J. Goedheer, *IEEE Trans Plasma Sci.* **19**, 170 (1991).
22. M.A. Lieberman, Electronics Research Laboratory, College of Engineering, University of California, Berkeley, CA 94720, Memorandum No. UCB/ERL M87/65, 1987.
23. D.L. Flamm, *J. Vac. Sci. Technol. A* **4**, 729 (1986).
24. K. Köhler, J.W. Coburn, D.E. Horne, E. Kay, and J.H. Keller, *J. Appl. Phys.* **57**, 59 (1984).

25. A. Boschi and F. Magistrelli, *Nuovo Cimento* **29**, 487 (1963).
26. K.-U. Riemann, *J. Appl. Phys.* **65**, 999 (1989).
27. S. Biehler, *Appl. Phys. Lett.* **54**, 317 (1989).
28. M.A. Lieberman and S.E. Savas, *J. Vac. Sci. Technol. A* **8**, 1632 (1990).
29. J.H. Tsai and C. Wu, *Phys. Rev. A* **41**, 5626 (1990).
30. M.A. Lieberman, *J. Appl. Phys.* **65**, 4186 (1989).
31. L. Tonks and I. Langmuir, *Phys. Rev.* **34**, 876 (1929).
32. E.R. Harrison and W.B. Thompson, *Proc. Phys. Soc.* **74**, 145 (1959).
33. J.H. Ingold, *Phys. Fluids* **15**, 75 (1972).
34. V. Vahedi, M.A. Lieberman, M.V. Alves, J.P. Verboncoeur, and C.K. Birdsall, *J. Appl. Phys.* **69**, 2008 (1991).
35. V.A. Godyak and Z.Kh. Ganna, *Sov. J. Plasma Phys.* **6**, 372 (1980).
36. V.A. Godyak and N. Sternberg, *Phys. Rev. A* **42**, 2299 (1990).
37. C. Wild and P. Koidl, *J. Appl. Phys.* **69**, 2909 (1991).
38. C.D. Child, *Phys. Rev.* **32**, 492 (1911).
39. A.J. van Roosmalen and P.J.Q. van Voorst Vader, *J. Appl. Phys.* **68**, 1497 (1990).
40. *CRC Standard Mathematical Tables*, 24th edition (CRC Press, Cleveland, Ohio, 1976), p.85.
41. V.A. Godyak, R.B. Piejak, and B.M. Alexandrovich, *Rev. Sci. Instrum.* **61**, 2401 (1990).
42. M. Surendra and D.B. Graves, *IEEE Trans. Plasma Sci.* **19**, 144 (1991).
43. D. Vender and R.W. Boswell, *IEEE Trans. Plasma Sci.* **18**, 725 (1990).
44. Ph. Belenguer and J.P. Boeuf, *Phys. Rev. A* **41**, 4447 (1990).
45. J.P. Boeuf, *Phys. Rev. A* **36**, 2782 (1987).
46. M.S. Barnes, T.J. Colter, and M.E. Elta, *J. Appl. Phys.* **61**, 81 (1987).
47. G.A. Hebner and J.T. Verdeyen, *IEEE Trans. Plasma Sci.* **14**, 132 (1986).
48. C.M. Horwitz and T. Puzzer, *J. Vac. Sci. Technol. A* **8**, 3132 (1990).
49. M.V. Alves, V. Vahedi, and C.K. Birdsall, *Bull. Am. Phys. Soc.* **34**, 2028 (1989).
50. C.M. Horwitz, *J. Vac. Sci. Technol.* **1**, 60 (1983).



## FIGURE CAPTIONS

Figure 1. (a) The asymmetric capacitively coupled rf discharge. (b) Illustration of the sheath. The electrode is at  $x = 0$ ; the glow is to the right. The electron sheath edge moves from the maximum position  $x = x_m$  to a minimum position near  $x = 0$ . The ion density at the  $x_m$  is  $n_s$ .

Figure 2. Current waveforms for  $U_1 = 300$  and  $n_s = 10^{10} \text{ cm}^{-3}$  at area ratios  $\beta$  of 1, 2.1, and 4. Each curve is labeled with its area ratio. Also plotted is the single sheath current waveform, labeled "single."

Figure 3. Frequency spectrum of the current waveforms for  $U_1 = 300$  and  $n_s = 10^{10} \text{ cm}^{-3}$  at area ratios of 1 (dots), 2.1 (squares), and 8 (triangles): (a) the spectrum for the total current; (b) the spectrum for the conduction current at the powered electrode (sheath A).

Figure 4. Single sheath current waveforms for  $U_1 = 300$  and  $n_s = 10^{10} \text{ cm}^{-3}$ : (a) using a Child law ion density; (b) using a uniform ion density  $n_s = 23 \times 10^{10} \text{ cm}^{-3}$ . The displacement, conduction and total currents are labeled  $J_d$ ,  $J_c$  and  $J_T$  respectively.

Figure 5. Current waveform from the two-sheath model for  $U_1 = 300$  and  $n_s = 23 \times 10^{10} \text{ cm}^{-3}$  at an area ratio  $\beta = 2.1$ . This shows the effect of the increased size of the conduction current relative to the displacement current, at a ratio that can occur in a nonuniform ion density sheath. The displacement, conduction and total currents are labeled  $J_d$ ,  $J_c$  and  $J_T$  respectively.

Figure 6. Two-sheath model results: (a) Sheath voltage  $U_A$ , and (b) current waveforms for area ratio  $\beta=1$ ,  $U_1 = 300$  and  $n_s = 23 \times 10^{10} \text{ cm}^{-3}$ . The displacement, conduction and total currents are labeled  $J_d$ ,  $J_c$  and  $J_T$  respectively.

Figure 7. Two-sheath model current waveforms for area ratio  $\beta = 1$ ,  $U_1 = 250$ ,  $n_s = 3 \times 10^9 \text{ cm}^{-3}$ , a frequency of 1.5 MHz, and an ion mass of 4 amu. The triangular waveform is similar to the result in Fig. 6 of Ref. 42. The displacement, conduction and total currents are labeled  $J_d$ ,  $J_c$  and  $J_T$  respectively.

Figure 8. (a) Experimental data for the rf part of the discharge voltage  $V$  and the discharge current  $I$  from a confined argon discharge at 70 mtorr and 10 MHz. (b) Fourier spectrum of the current.

Figure 9. Two-sheath model results for the current waveform when the external voltage is sinusoidal (dashed line, labeled "sine  $V(t)$ "); and when the voltage waveform from Figure 8 is used, and the current waveform is truncated above the sixth harmonic (solid line, labeled "Exp't  $V(t)$  & truncated"). The density parameter is  $23 \times 10^{10} \text{ cm}^{-3}$  and the positive peak value of the rf part of the external voltage was  $U_1 = 300$ .

Figure 10. DC bias  $U_0$  vs. rf amplitude  $U_1$  in the two-sheath model. Curves from the resistive-capacitive sheath model with  $n_s = 10^9 \text{ cm}^{-3}$ : (A) area ratio  $\beta = 2.1$ ; and (C)  $\beta = 10$ . Curves from the pure resistive sheath model: (B)  $\beta = 2.1$ ; and (D) single sheath limit ( $\beta \gg 1$ ).

Figure 11. Sheath voltage ratios: (a) the dc ratio  $U_A^{(0)}/U_B^{(0)}$ ; and (b) the first harmonic ratio  $U_A^{(1)}/U_B^{(1)}$ . Curves from the resistive-capacitive sheath model with  $n_s = 10^9 \text{ cm}^{-3}$ : (A)  $U_1 = 300$  (solid), and (C)  $U_1 = 30$  (dashed). Curves from the pure resistive sheath model: (B)  $U_1 = 300$  (solid), and (D)  $U_1 = 30$  (dashed). The dashed straight line with slope of 2 represents the quadratic scaling with area ratio from simple arguments.

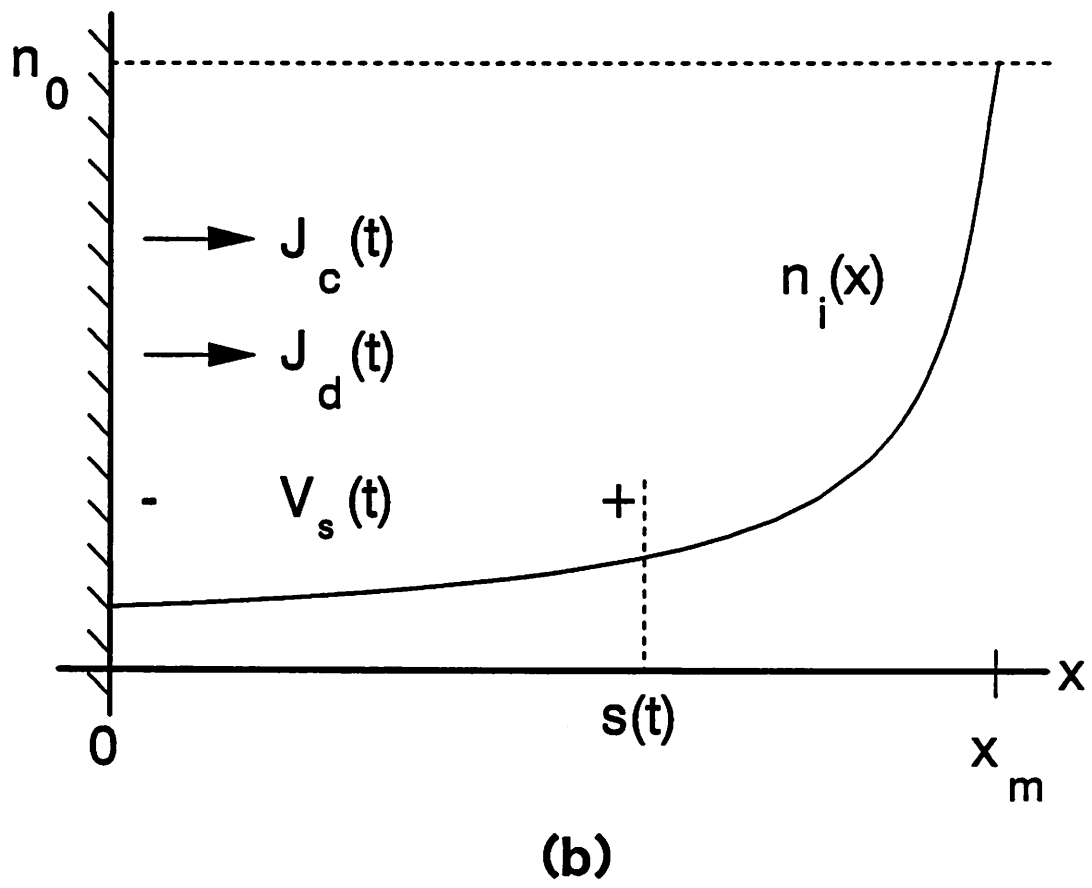
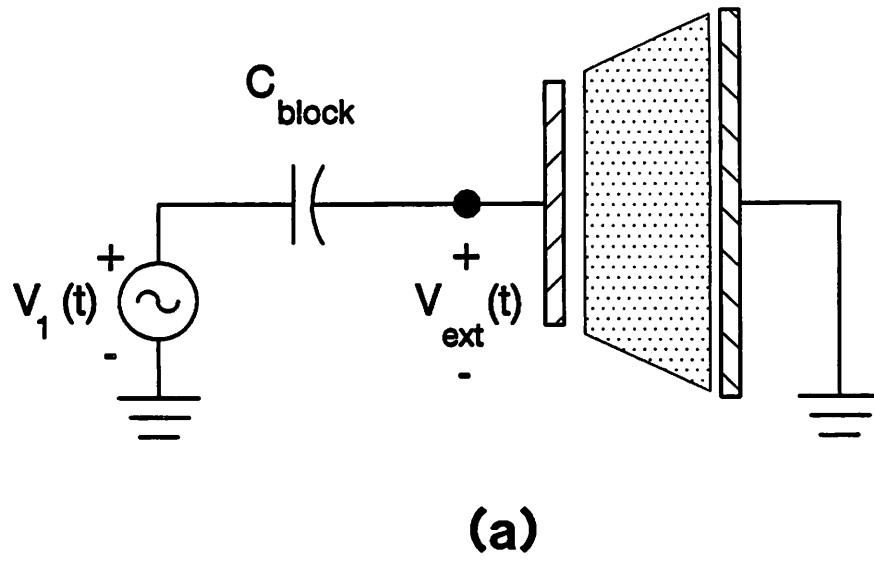


Figure 1

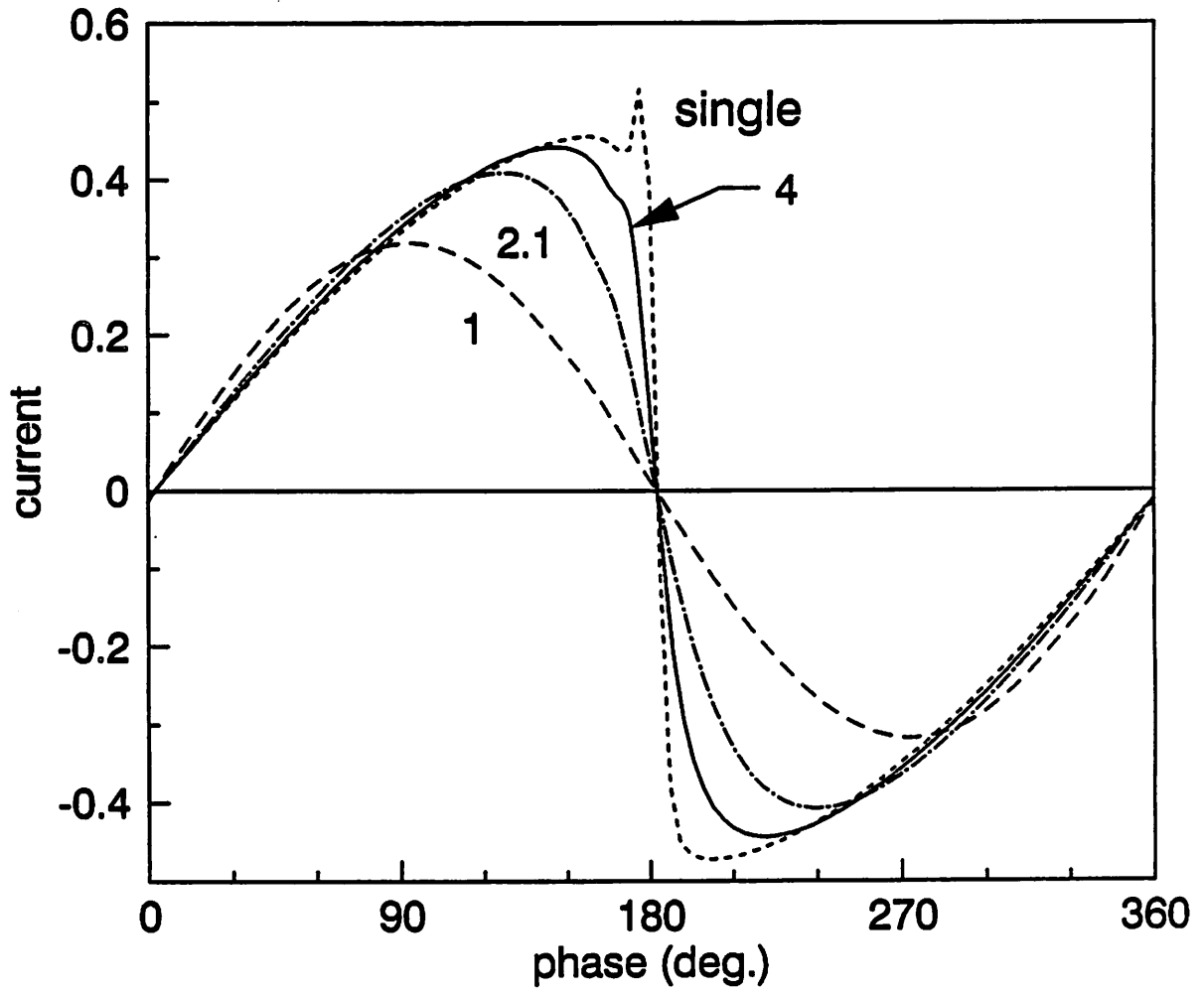


Figure 2

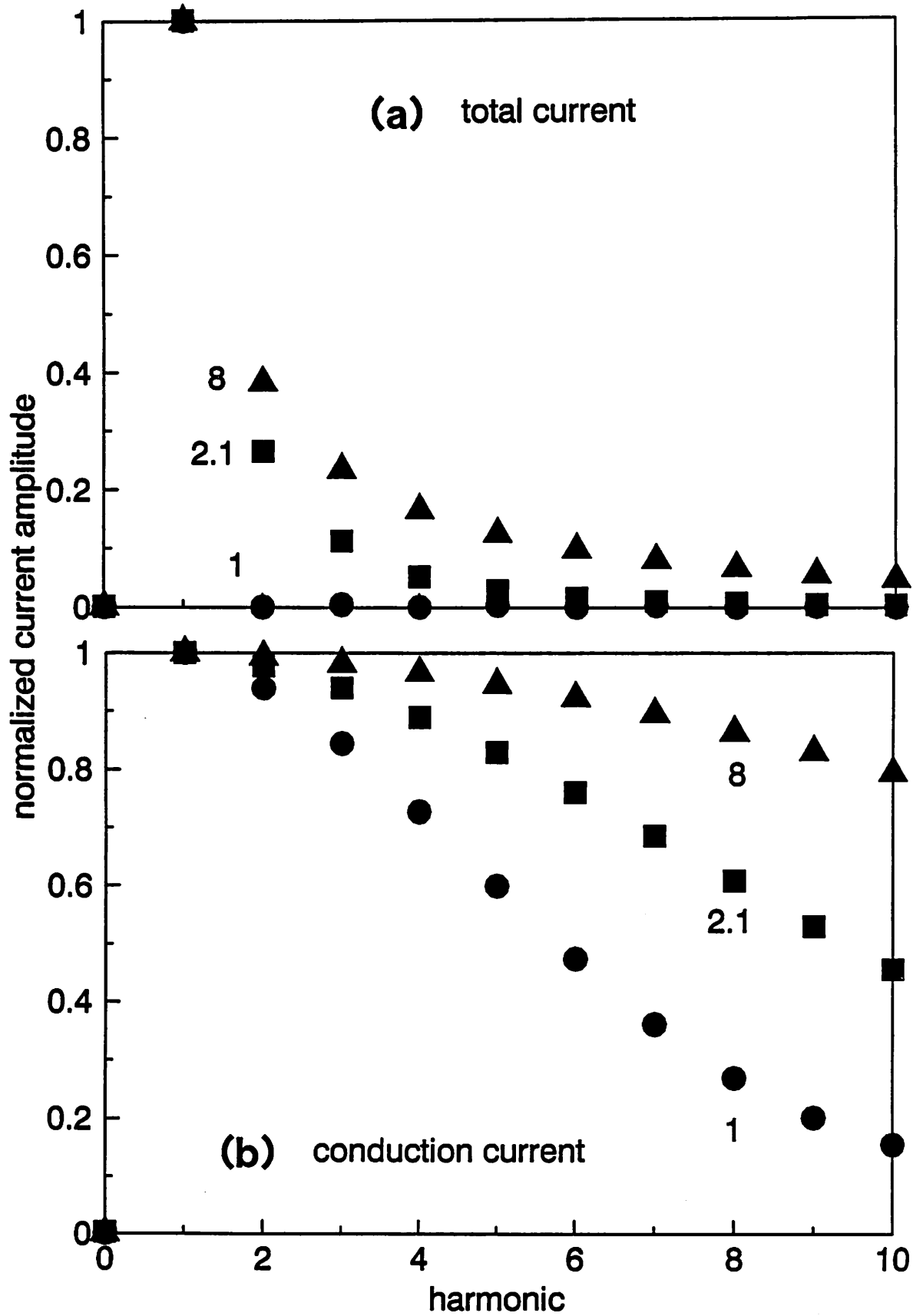


Figure 3

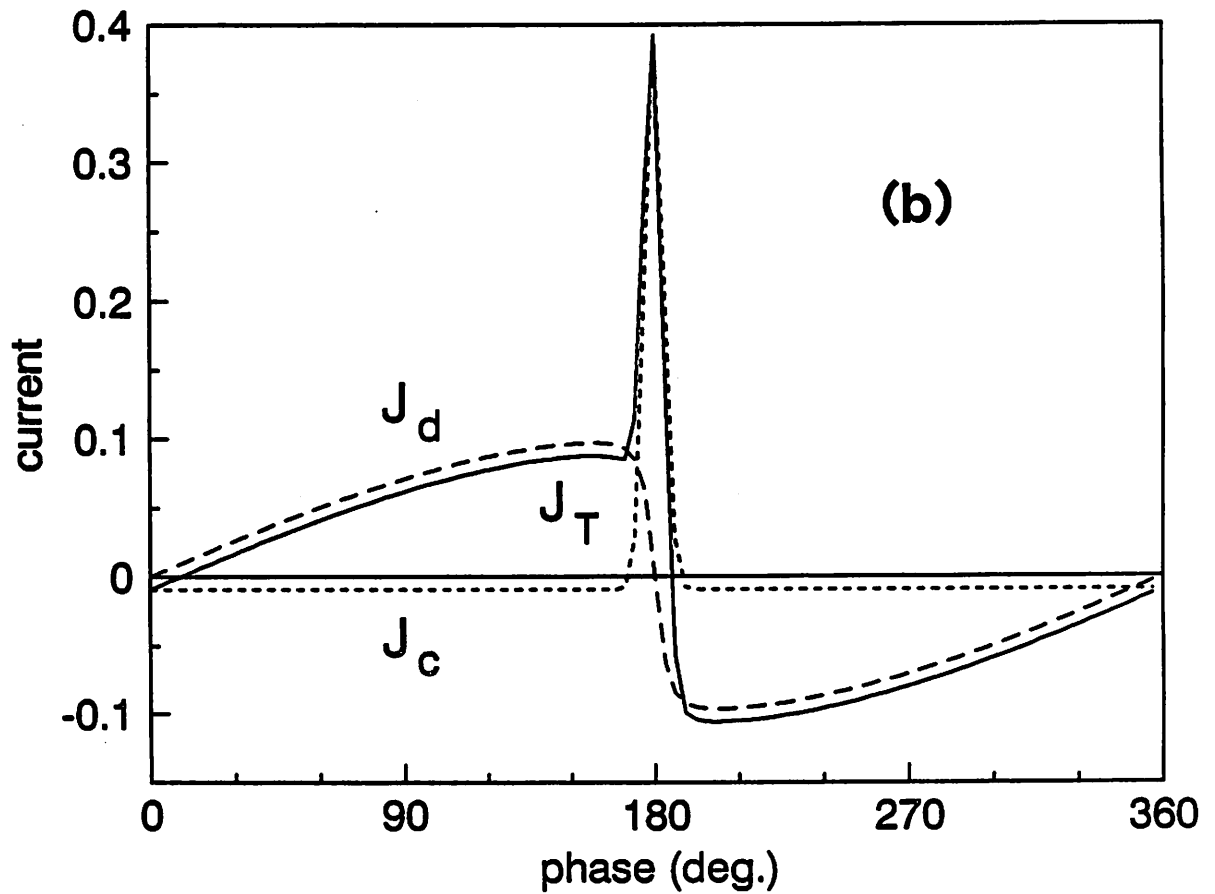
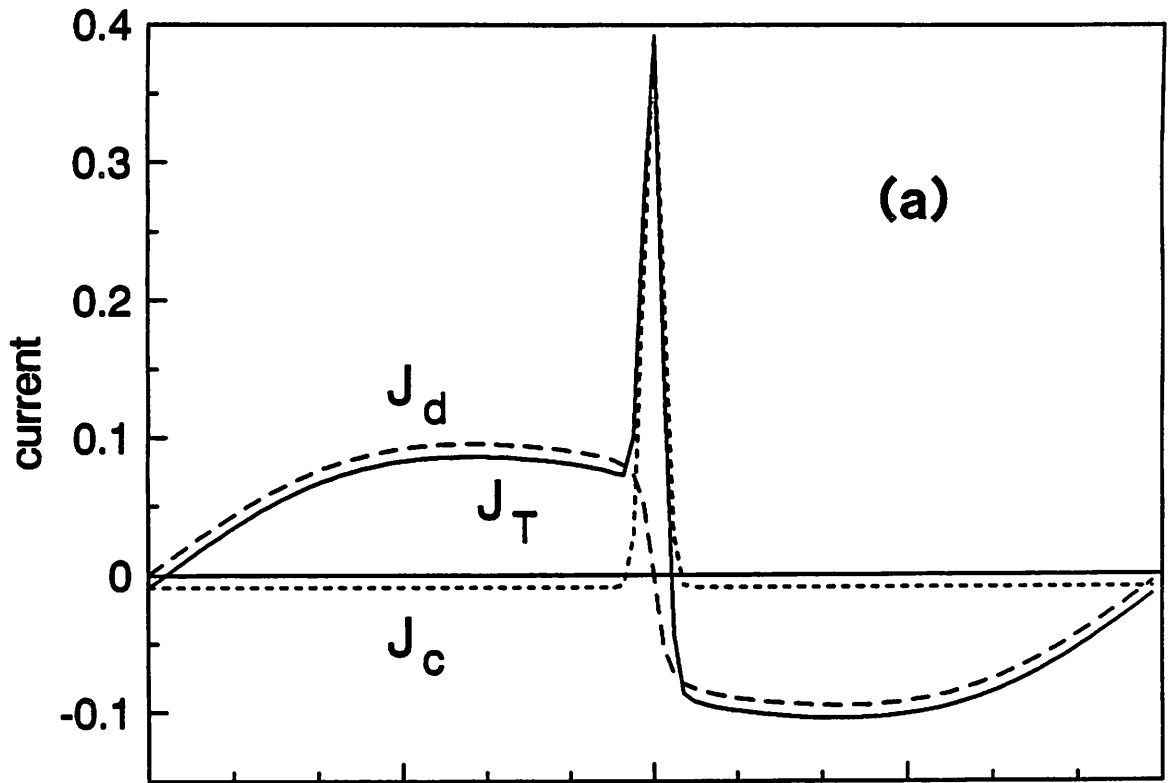


Figure 4

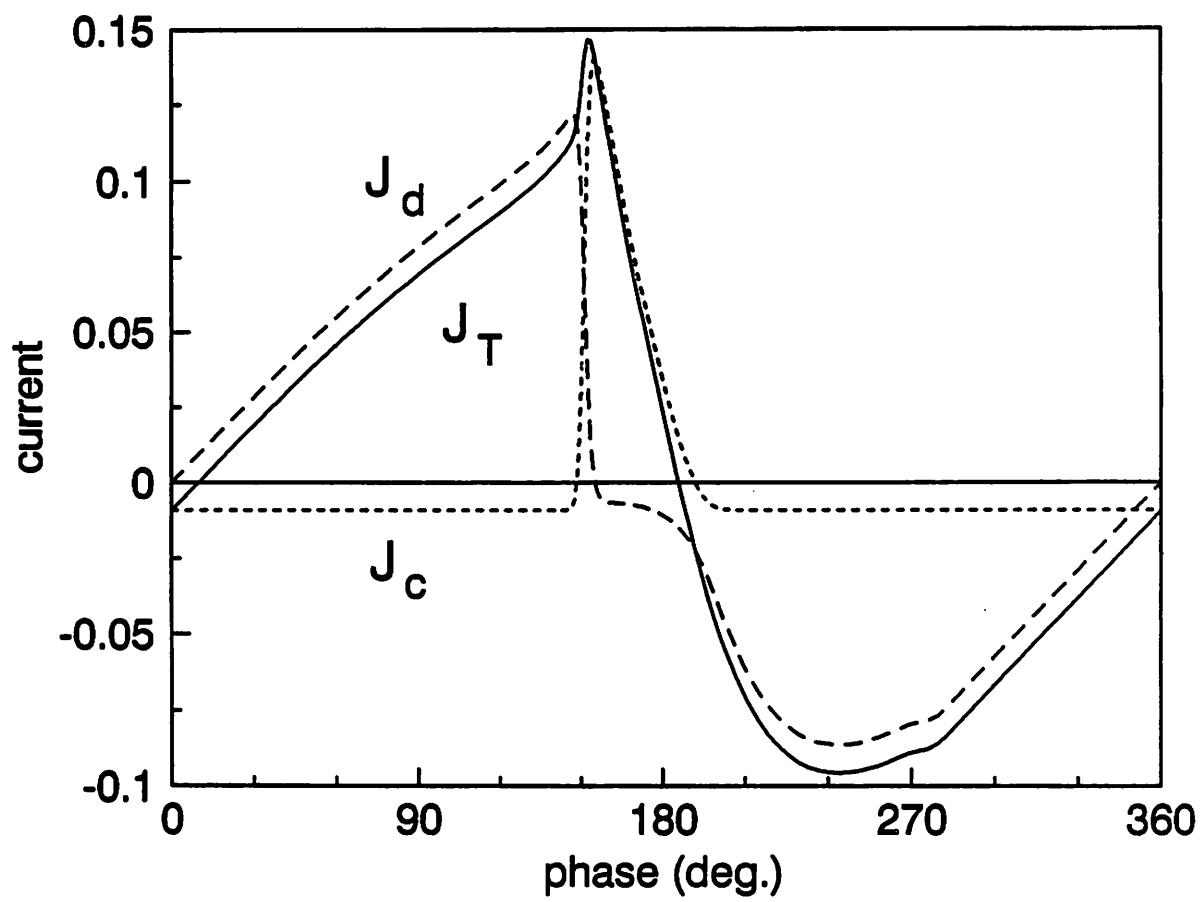


Figure 5

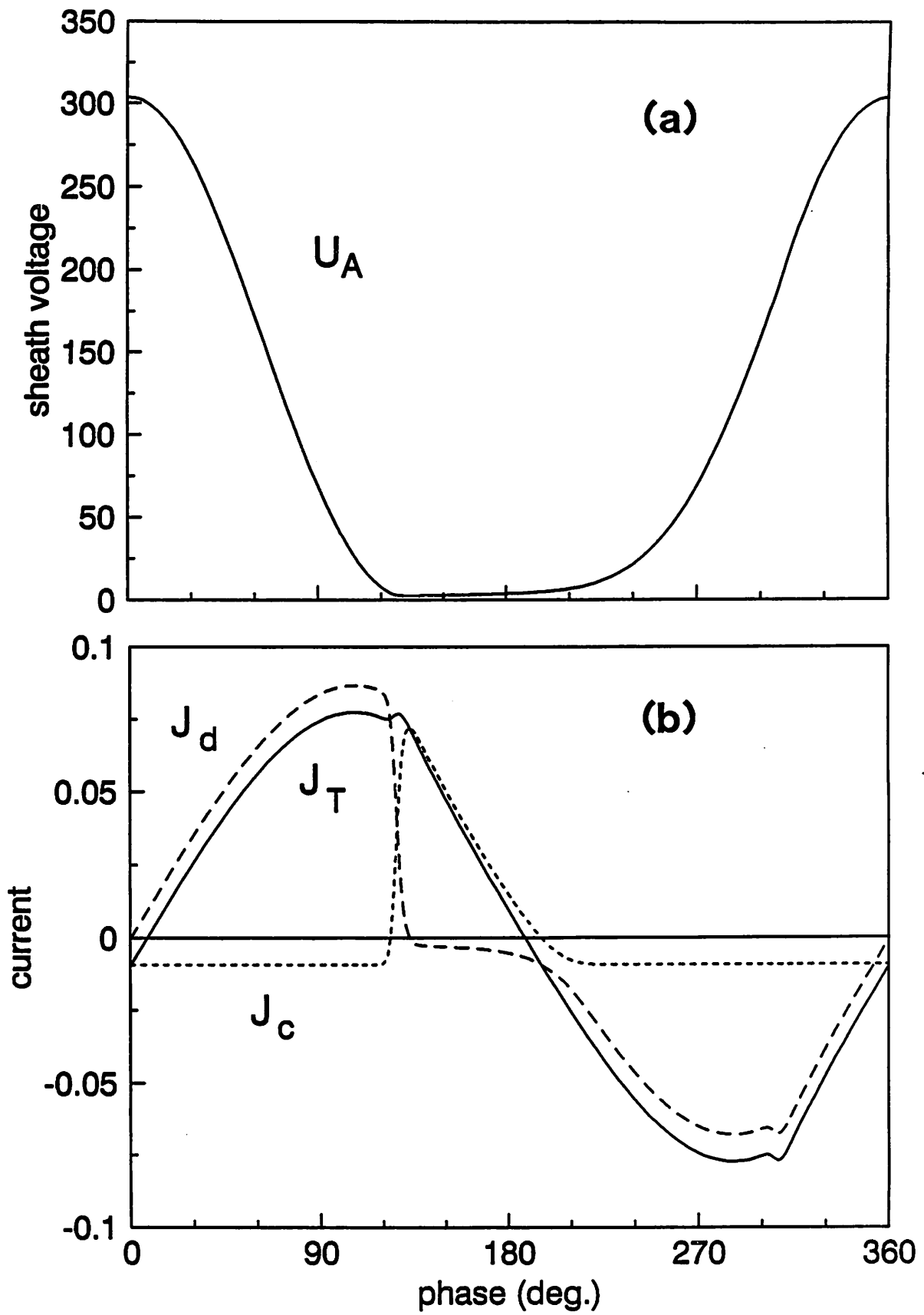


Figure 6

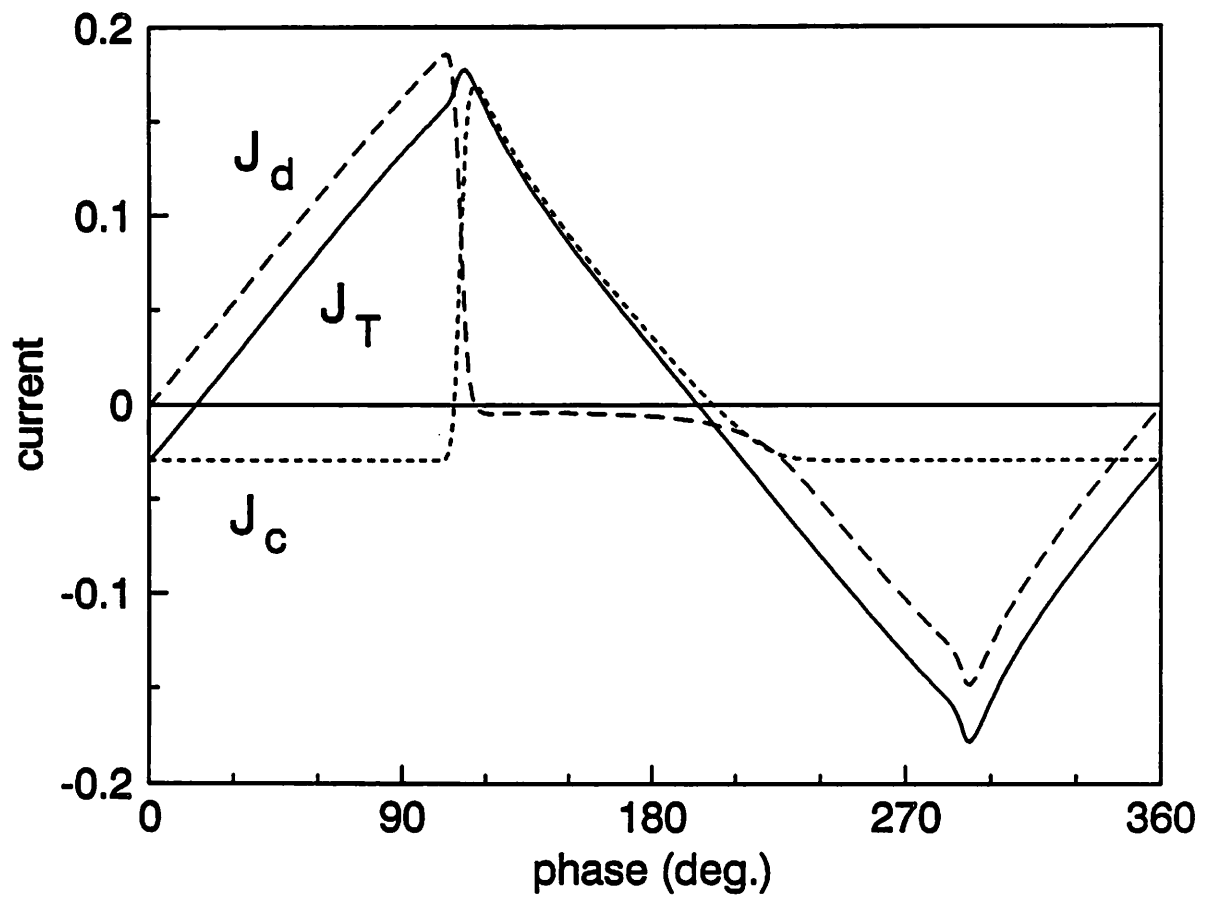


Figure 7

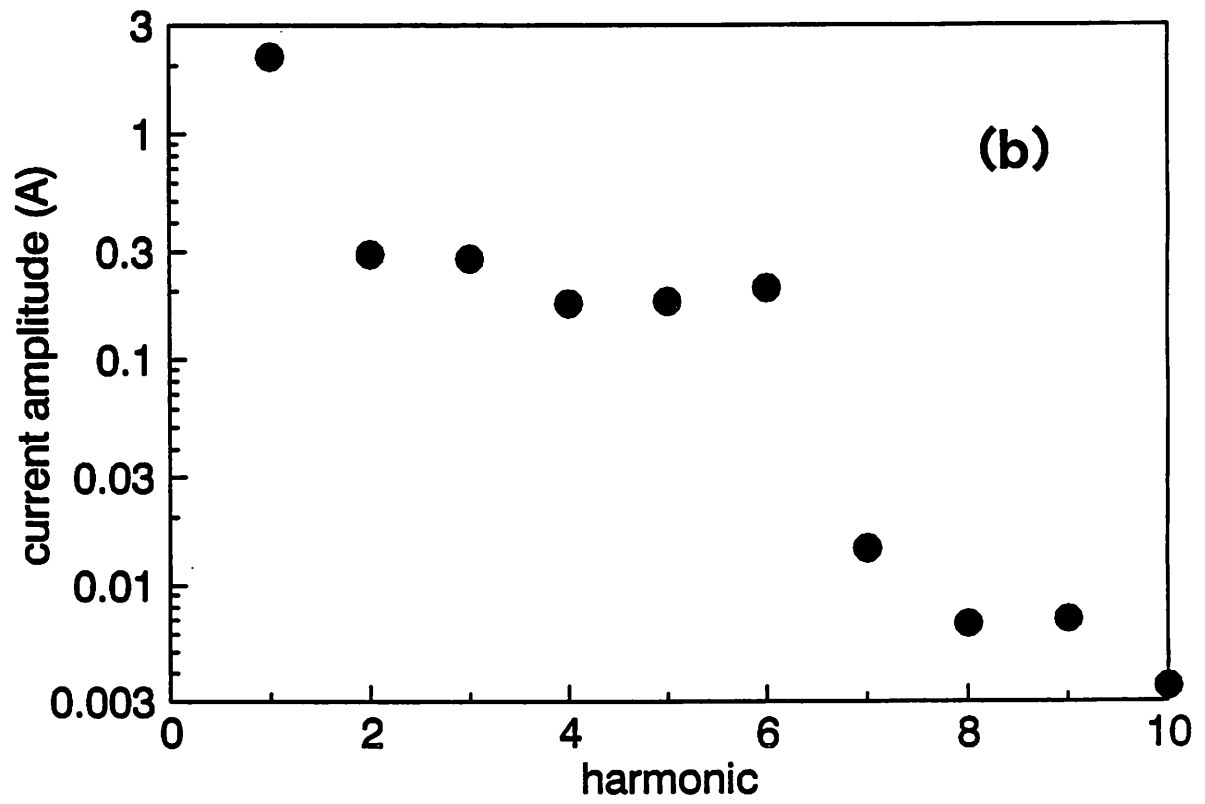
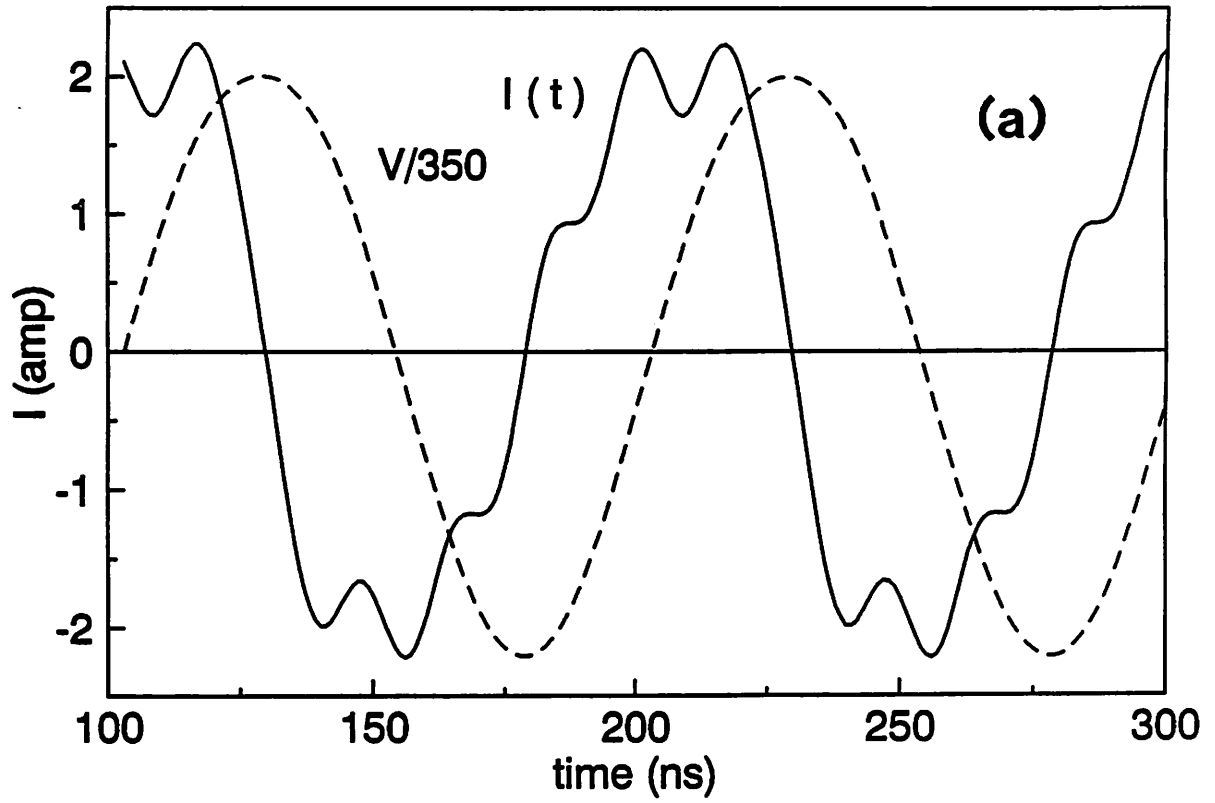


Figure 8

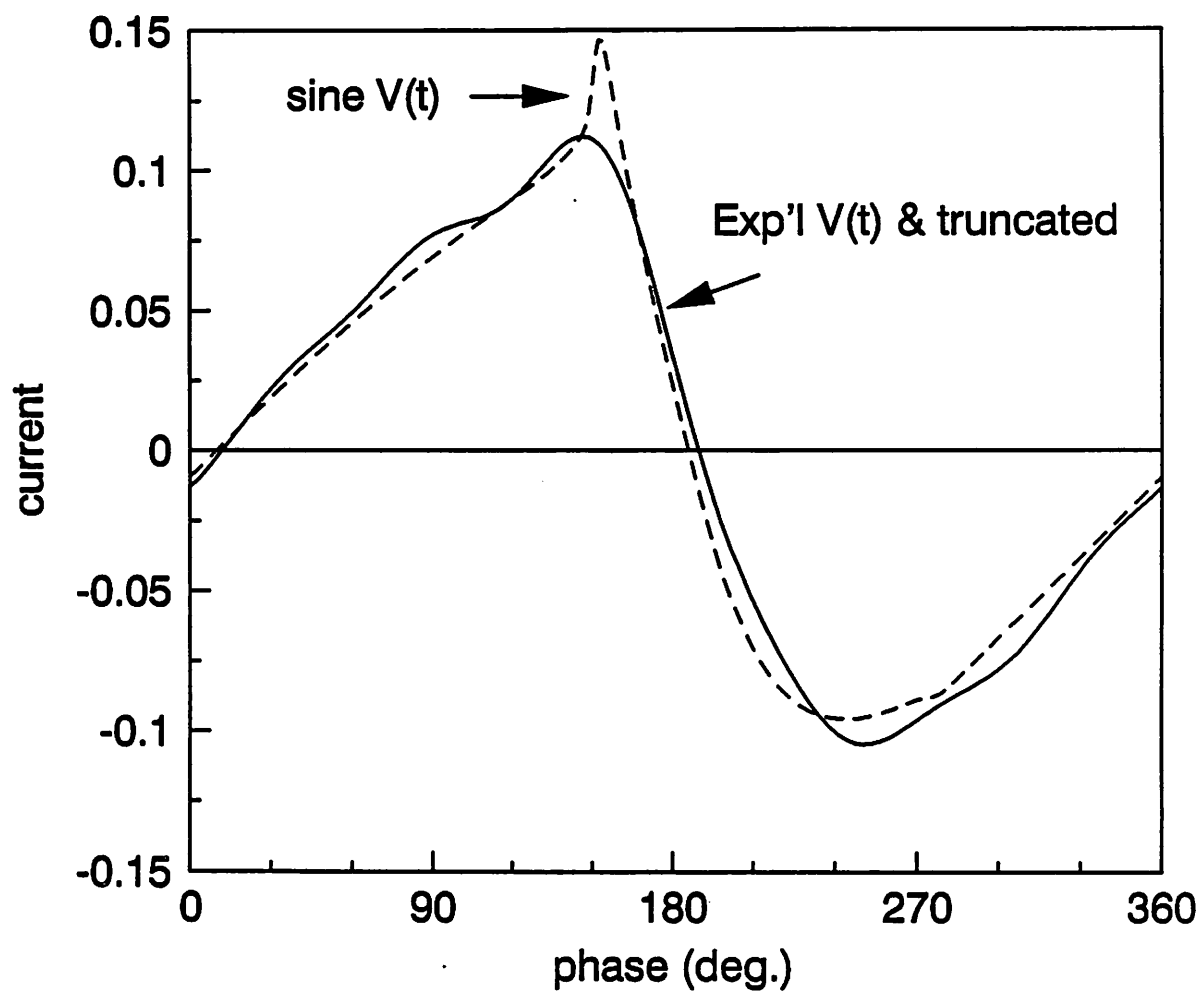


Figure 9

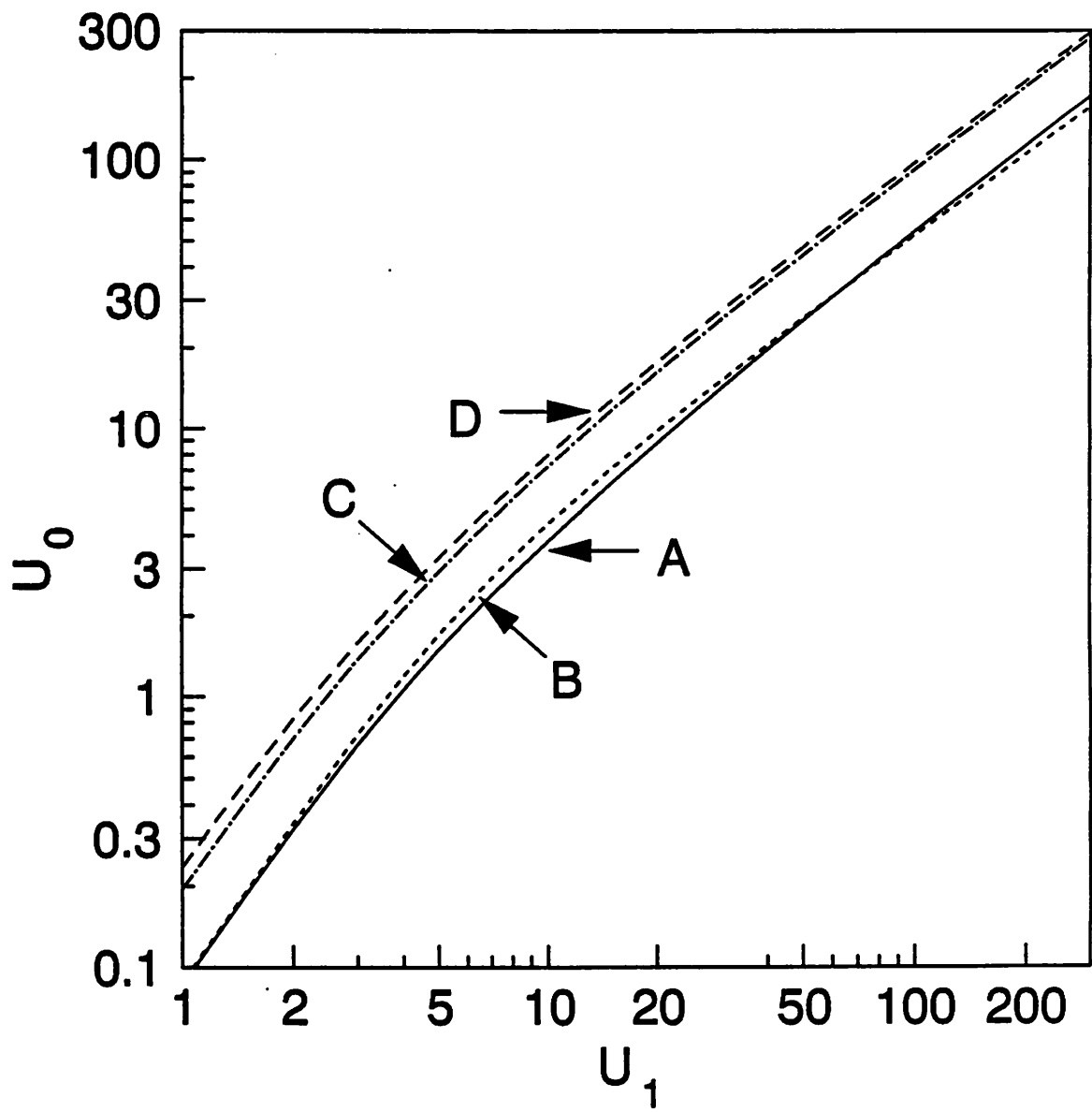


Figure 10

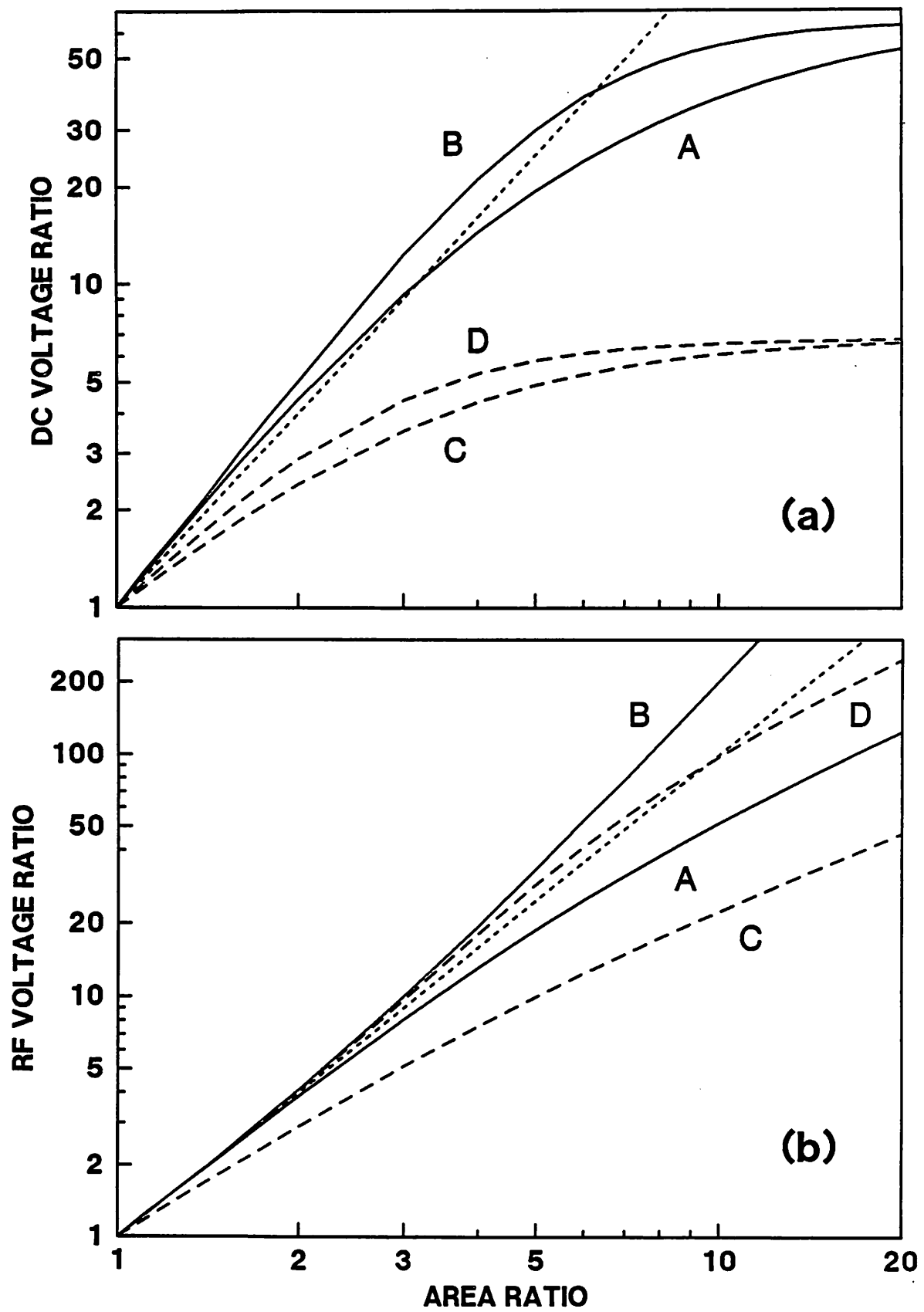


Figure 11